



Effects of Variable Total Pressures on Instability and Extinction of Rotating Detonation Combustion

Majie Zhao¹ · Jiun-Ming Li² · Chiang Juay Teo^{1,2} · Boo Cheong Khoo^{1,2} ·
Huangwei Zhang¹

Received: 4 January 2019 / Accepted: 4 July 2019/Published online: 19 July 2019
© Springer Nature B.V. 2019

Abstract

Instability, extinction and re-initiation of rotating detonation in a two-dimensional Rotating Detonation Engine (RDE) configuration are numerically investigated, and the emphasis is laid on the effects of variable total pressures on the above combustion dynamics. Two conditions, i.e. different constant pressures and time-varying pressures, are considered to investigate the combustion instability in RDE. It is seen that under constant pressure condition the rotating detonation is more prone to instability at low pressure, due to the instability from the deflagrative surface. The intrinsic frequency for the unstable cases with different pressures is close, and maybe related to the RDE configuration and/or fuel properties. For the time-varying pressures with various specified frequencies, the RDE shows the different levels of instability characterized by multiple frequencies. The dominant frequencies vary, depending on the competition between the forced external frequency and the intrinsic one induced by the RDE system. About the extinction of continuously rotating detonation, it can be found that when the total pressure is reduced to a relatively lower value the detonation is quenched and left with deflagrative combustion. Furthermore, when the total pressure is increased based on the extinguished flow fields, detonation fronts are re-initiated due to the local high pressure. The stochasticity in RDE re-initiation has been found, in terms of the location and number of initial detonation front, the propagation direction, their interaction and final stabilization.

Keywords Rotating detonation combustion · Variable total pressures · Combustion instability · Detonation extinction · Detailed chemical mechanism

✉ Huangwei Zhang
huangwei.zhang@nus.edu.sg

Majie Zhao
mpezma@nus.edu.sg

¹ Department of Mechanical Engineering, Faculty of Engineering, National University of Singapore, 9 Engineering Drive 1, Singapore 117576, Republic of Singapore

² Temasak Laboratories, National University of Singapore, 5A Engineering Drive 1, #09-02, Singapore 117411, Republic of Singapore

1 Introduction

Pressure Gain Combustion (PGC) can considerably increase the thermal efficiency compared to the conventional combustion process with constant pressure. One of the forms to realize PGC is to introduce either a constant volume or detonation mode of combustion. As a potential detonation propulsion system, Rotating Detonation Engine (RDE), which utilizes the high-efficiency detonation propagation to sustain the combustion process, has attracted more and more attention from both scientific and engineering communities over the past few years [1–3].

Overall, nowadays there are still many challenges in designing a practical RDE combustor, e.g. ignition of detonation, detonation stability and perfect mixing of fuel and air. Besides, since both detonation and deflagration modes occur in the RDE chamber, the interactions between these two modes are strong and therefore render the combustion dynamics in RDE complicated. In recent years, RDE has been studied through experiments and numerical simulations on numerous aspects, including different fuels [4], fuel inflow rates [5], equivalence ratios [6], ratios of throat area to wall area [7, 8], ratios of inflow stagnation pressure to backpressure [6, 9], RDE combustor channel width [10, 11] and geometry [12–14]. Some recent works on RDE are reviewed in detail by Zhou et al. [1], Kailasanath [2], Lu [3] and Anand and Gutmark [15].

Based on the aforementioned work, one can see that the experimental measurements are relatively difficult to be performed to obtain the detailed flow and combustion field structures. Therefore, the role of numerical simulations in RDE investigations becomes significant. In particular, with the fast development of high-performance computers, numerical simulations have gradually demonstrated its ability to provide the detailed flow and detonation fields to better understand the fundamental physics and performance potential of the generic rotating detonation-wave engine. For example, Schwer et al. [4] study the fluid dynamics of RDEs with hydrogen and hydrocarbon fuels and found that the thermodynamics of the different fuels are the main factors that influences the RDE behaviors. The three-dimensional thrust performance analysis of RDE are performed by Jourdaine et al. [16] via numerical simulations. Also, a series of numerical simulation studies have been performed by Wang and co-workers [14, 17, 18], who showed that rotating detonation waves can be realized ranging from subsonic to hypersonic injection. Furthermore, parameters including stagnation pressure, stagnation temperature, injection area ratio, axial chamber length effects and the number of detonation waves on the performance of RDE are studied using one-step chemical reaction model with two-dimensional and three-dimensional RDE model by Yi et al. [19, 20] and Yamada et al. [21].

Recently, instabilities in the RDE have been observed in some experimental studies [22–24] and numerical simulations [25–29], which are also reviewed in detail by Anand and Gutmark [15]. Pressure-time trace from the experimental study of Anand et al. [24] indicates that there are four different instability modes in the RDE combustor, including the chaotic instability, waxing and waning instability with low frequency, transient mode switching, and the Longitudinal Pulsed Detonation (LPD) instability. The longitudinal pulsed detonation instability has been studied in great detail by Anand et al. [22]. It is found that the air injection pressure ratio is one of the important factors to determine the LPD instability. Specifically, it occurs when the air injection pressure ratio is between 1.4 and 1.85 in their experiments, while for low air injection pressure ratio (below 1.2), chaotic detonation propagation and re-ignition of the detonation wave are observed. A sudden wave reversal is also observed in some experimental works [30, 31]. In these experimental studies, there may be different factors inducing the unstable detonation propagation, e.g. the local turbulence and/or insufficient mixing between

fuel and oxidizer. Therefore, it would be probably difficult to isolate the stagnation pressure effects and further understand how they intrinsically affect the detonation instability.

Lu et al. emphasize that the deflagration front may destabilize the detonation front through affecting the height of the latter and hence making it degrade into deflagration front [3]. Through simulating the two-dimensional domain, Hishida et al. analyze the K–H instability on the interface in rotating detonation combustion [29]. They also observe the local explosion along the unstable contact surfaces with ripple structures. Li and his co-workers numerically analyze the interface instability between the fresh mixture and burned products in two-dimension RDE domain [27]. They find that besides the K–H instability, two other mechanisms may also induce the interface instability, including Rayleigh–Taylor (R–T) instability and baroclinic torque. Besides the interface instability, numerical results by Liu et al. [26] show that the instability observed in their work result from the interactions between dual rotating detonation waves in the RDE chamber. In the foregoing work, the RDE total pressures are also assumed to be constant (e.g. 30 atm by Liu et al. [26] and 3.5 atm by Li et al. [27]) and therefore their effects on RDE instability are not examined.

There are some investigations available on how the variable total pressure affects the rotating detonation dynamics. For instance, Schwer and Kailasanath discuss how the varied total pressures influence the performance of the considered injection systems [32, 33]. Levin et al. investigate the response of the chamber pressure to the changing total pressure from the RDE inlet [34]. From the above studies [32–34], one can see interesting transient behaviors related to the inlet total pressure, e.g. detonation failure and re-initiation. However, destabilization of deflagration and detonation fronts subject to the varying total pressure have not been particularly discussed above.

In this paper, we aim to investigate the two-dimensional RDE with variable upstream total pressures, to understand the critical combustion dynamics in RDE system, including instabilities, extinction and re-initiation. The emphasis is laid on the influences of the variable total pressures on both deflagrative and detonative front instabilities, as well as RDE extinction and re-initiation. Compared to the existing studies about RDE instability [22–28], the novelty of the current work includes: (1) the forced perturbations of the total pressure mimicking the high-frequency variations of the propellant supply from the upstream plenum in the practical RDE system are considered; (2) extinction and re-ignition of detonation fronts due to the varied total pressures are discussed; and (3) the necessity to accurately predict both deflagrative and detonative fronts simultaneously in RDE instability simulation is emphasized. Meanwhile, we also briefly discuss the stochastic characteristics of detonation re-initiation, which may be the topic of our future work. The rest of the paper is organized as follows: in Section 2, governing equations and physical model are presented. The numerical results are presented and discussed in Section 3. Finally, the main conclusions drawn from our work are summarized in Section 4.

2 Governing Equation and Physical Model

2.1 Governing equation

For high-speed combustion, the molecular viscosity, thermal conduction and mass diffusion can be neglected without loss of the main characteristics of the flow and scalar fields.

Therefore, similar to the previous work, e.g. in Refs. [9, 25, 28, 35, 36], Euler equations together with species mass fraction equations are solved in the present simulations, which read

$$\frac{\partial \rho}{\partial t} + \nabla \cdot (\rho \mathbf{u}) = 0, \quad (1)$$

$$\frac{\partial(\rho \mathbf{u})}{\partial t} + \nabla \cdot (\rho \mathbf{u} \mathbf{u}) + \nabla p = 0, \quad (2)$$

$$\frac{\partial(\rho Y_m)}{\partial t} + \nabla \cdot (\rho \mathbf{u} Y_m) = \dot{\omega}_m \quad (m = 1, \dots, N), \quad (3)$$

$$\frac{\partial(\rho E)}{\partial t} + \nabla \cdot (\rho \mathbf{u} E) + \nabla \cdot (\mathbf{u} p) = \dot{\omega}_T, \quad (4)$$

where t is time and $\nabla \cdot (\cdot)$ is divergence operator in Cartesian coordinate. N is the number of species. The variables ρ , \mathbf{u} , $E (= e + |\mathbf{u}|^2/2)$, p , Y_m and T are the density, velocity vector, total energy, pressure, mass fraction of m -th species and temperature, respectively. Here e is internal energy. Note that no body forces (like gravity force) are considered in the current work. Pressure is calculated through the equation of state

$$p = \rho R T. \quad (5)$$

Here R is specific gas constant of a mixture and is calculated from the molar gas constant divided by the molar mass (M) of the mixture, i.e. $R = R_u / M$, where R_u is universal gas constant. In addition, $\dot{\omega}_m$ and $\dot{\omega}_T$ ($\equiv \sum_{m=1}^N \dot{\omega}_m h_m$, h_m is the total enthalpy of m -th species) in Eqs. (3) and (4) are the chemistry-related source terms in the species mass fraction equations (Eq. 3) and energy equation (Eq. 4), respectively. They account for the generation/destruction of species and heat release from combustion, respectively.

The governing equations from Eqs. (1)–(4) are discretized with finite volume method and solved by the *RYrhoCentralFoam* solver, which is developed from the fully compressible flow solver *rhoCentralFoam* in the framework of OpenFOAM 5.0 [37]. The second order implicit backward method is employed for temporal discretization and the time step is adjusted to ensure that the maximum Courant number (i.e. CFL number) is less than 0.1. Second-order Godunov-type central and upwind-central schemes following Kurganov [38] and Kurganov et al. [39] are used to discretize the convection terms in Eqs. (1)–(4). The chemical source terms in Eqs. (3) and (4) are efficiently solved with Euler implicit method.

2.2 RDE configuration, computational domain, boundary and initial conditions

Because the annular RDE chamber width (typically several millimeters) is very small compared to its diameter, the computational domain of RDE can generally be “unrolled” into a two-dimensional one due to the limited radial variation within the flow. This simplification has also been adopted by numerous previous work (e.g. Refs. [9, 26–28], to name a few) to reduce the computational cost, and meanwhile the main characteristics of the combustion dynamics

(e.g. detonation propagation speed) and flow patterns (e.g. shock wave evolutions) can still be predicted sufficiently well compared to those from the full three-dimensional simulations. Note that the three-dimensional effects (e.g. wall heat loss, lateral relief, etc.) on rotating detonation combustion may become critical under some scenarios, e.g. with low pressure ratio [40] and finite channel width [41]. However, the above effects are expected to be not dominant in the current work. Therefore, in the current computations, a rectangular computational domain (see Fig. 1) is used to mimic the originally annular RDE combustor. Its length is assumed to be 280 mm (equivalent to the circumference of the middle plane of 3D combustor), whereas the height is 100 mm (equivalent to the height of the typical 3D RDE). These scales are larger than those used in previous two-dimensional RDE instability simulations, e.g. 120 mm \times 90 mm by Liu et al. [26] and 100 mm \times 40 mm by Li et al. [27]. Ours are closer to those of the practical RDE chambers, e.g. the ones investigated numerically by Palaniswamy et al. [8] and experimentally by Bluemner et al. [23].

The domain in Fig. 1 is discretized with 352,800 Cartesian cells. In the base case (i.e. Case 2 in Table 1), the minimal size is 0.2 mm in the x -direction. For y -direction, it is stretched from 0.1 mm at the headwall end to 1 mm at the outlet with the stretching ratio $\varrho=10$. These resolutions are not expected to resolve the detailed detonation structures (the induction length in the calculated ZND structure is about 0.2 mm with initial temperature 300 K and initial pressure 1 atm based on the chemical mechanisms given in Section 2.3 and Shock & Detonation Toolbox [42]). The similar resolutions (0.1 or 0.2 mm) are also used in Refs. [26, 27, 29], in which the main structures for RDE instability analysis can be captured well. The sufficiency of the mesh resolution for our simulations of RDE will be investigated in Section 3.1, through performing the mesh sensitivity analysis.

For the initial flow field, the computational domain is filled with stoichiometric H₂-air mixture. To achieve an initial propagating detonation front, a localized region with high temperature and pressure is initialized as shown in Fig. 1. In the two-dimensional domain (see Fig. 1), the left and right boundaries are assumed to be periodic and therefore the continuously rotating detonation combustion can be achieved. Non-reflective boundary condition is enforced for the outlet and the ambient pressure is 1 atm. Using this boundary

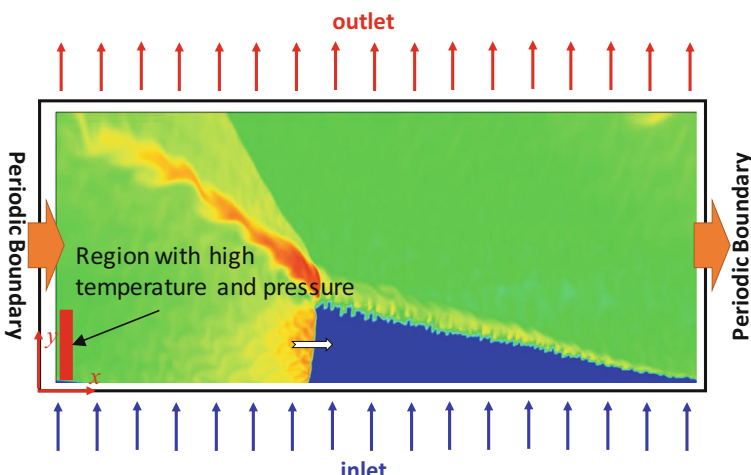


Fig. 1 Computational domain and boundary conditions in two-dimensional rotating detonation engine. The red rectangular region with high temperature and pressure is used for initiating the rotating detonation at $t=0$

Table 1 Information for the cases simulated*

Cases		Grid size Δx (mm)	Grid size** Δy (mm)	Inflow total pressure P_0 (atm)	Chemical mechanism
Constant total pressure P_0	1	0.4	0.2~2	40	9 species, 19 reactions [44]
	2	0.2	0.1~1	40	
	3	0.1	0.05~0.5	40	
	4	0.2	0.1~1	20	
	5	0.2	0.1~1	10	
	7	0.2	0.1~1	40	4 species,
	8	0.2	0.1~1	20	1 reaction
	9	0.2	0.1~1	10	[43]
	10	0.2	0.1~1	20 + $5 \sin(2\pi \times 6400 t)$	9 species, 19 reactions [44]
	11	0.2	0.1~1	20 + $5 \sin(2\pi \times 3200 t)$	
Time-varying total pressure P_0	12	0.2	0.1~1	20 + $5 \sin(2\pi \times 1600 t)$	

*The inflow total temperature T_o for all the cases listed here are 300 K

**In y -direction, the cells are continuously stretched from the RDE head end to outlet with cell expansion ratio $\varrho = \Delta y_{max}/\Delta y_{min} = 10$. For example, in Case 1, $\Delta y_{max}=2$ mm is the size of the last cell at the outlet, while $\Delta y_{min}=0.2$ mm is the first size of the first cell close to the head end

condition, we can avoid spurious wave reflections from the RDE outlet towards the upstream region where the detonation and deflagration waves exist. These reflected waves may directly interact and hence affect the deflagration fronts. This will lead to incorrect prediction of instability from the deflagration fronts, which would further result in unstable detonation propagation and even extinction. Therefore, this boundary is a simplification of the real RDE outlet. Premixed stoichiometric H₂ – air mixture (with initial total temperature of 300 K and various total pressures listed in Table 1) is injected into the combustor from the inlet (bottom) boundary. It should be noted that the inlet mass flow rate is determined by the inlet total pressure and temperature. The inflow conditions (parameterized by pressure p_i , temperature T_i and y -direction velocity v) are determined by the relations between inlet local pressure p extrapolated from the inner field to the headwall and total pressure P_o assuming isentropic expansion [9, 25, 26, 28]. Since the total temperature is fixed in all the simulations (i.e. 300 K), only the inlet total pressure affects the reactant injection. Generally, higher inlet total pressure would lead to higher static pressure immediately downstream of the RDE injector through which the pre-mixture is discharged into the chamber. Although this inflow condition based on isentropic expansion relation cannot consider the propagation of the high-pressure post-detonation gas into the nozzle, it is widely used due to its simplicity and also due to its ability to model the fuel injection configuration (e.g. Refs. [9, 25, 26, 28]). It is expected to be sufficient in the current work, since here we are mainly interested in the combustion dynamics in the RDE chamber, instead of the injection nozzles.

2.3 Chemical mechanism

In the present simulations, one-step [43] and detailed [44] chemical mechanisms of H₂ – air are used for simulating detonative and deflagrative combustion in RDE. They have been used in other previous investigations, e.g. Refs. [45, 46], and good accuracies are achieved. For the former, there are 4 species, whilst for the latter there are 19 elementary reactions and 9 species.

Ignition delay time computed from one-step and detailed mechanisms at low (2 atm) and high (33 and 64 atm) pressures is compared with the experimental data from Slack [47] and Ó Conaire et al. [48], as shown in Fig. 2. Overall, the results show good agreement with the experimental data for both mechanisms, although some discrepancies can be seen for the one-step mechanism at 64 atm. In addition, cellular structures formed by detonations in shock tube are also performed with the detailed mechanism. Figure 3(a)–(c) respectively shows the distributions of temperature and numerical smoked foil and cell size (length δx and width δy marked in Fig. 3b) as a function of initial pressure from the two-dimensional detonation tube simulations. The results in Fig. 3(c) also agree reasonably well with the experimental data by Desbordes [49], Engel et al. [50] and Zitoun et al. [51]. Therefore, the comparisons in Figs. 2 and 3 validate the chemical mechanisms which will be used for the following RDE simulations.

2.4 Cases simulated

The information of the simulated cases is tabulated in Table 1, including grid resolution, operating conditions as well as chemical mechanisms. For all the cases, the total temperature of the fuel mixture is 300 K. With these cases, different influences can be studied, e.g. mesh resolution, chemical mechanism and total pressure. The effects of time-varying total pressure on the continuously rotating detonation dynamics (corresponding to Section 3.4 below) are investigated through forcing total pressure P_o at the fuel inlet following a sinusoidal function with time, i.e.

$$P_o(t) = 20 + 5 \sin(2\pi \times f \times t). \quad (6)$$

In Cases 10, 11 and 12 listed in Table 1, the corresponding frequency f is $f=6,400$, $3,200$ and $1,600$ Hz, respectively. In our numerical experiments, $f=6,400$ Hz is selected as the base value to mimic the high frequency instability. This frequency is close to the detonation rotating frequency f_0 of the detonation front predicted from the constant pressure cases, i.e. Cases 1–9. Physically, this high frequency perturbations (thousands of Hertz) may result from many factors, e.g. the coupling between fluid dynamics, combustion and acoustics characteristics in practical propulsion systems (like gas turbines and rocket engines), as reviewed by Anand and Gutmark [15]. The pressure from 15 atm to 25 atm from Eq. (6) is a reasonable range to achieve continuously rotating combustion in our numerical simulations.

3 Results and Discussion

3.1 Mesh sensitivity analysis

Figure 4 shows the temperature distributions predicted with three different grids corresponding to Cases 1, 2 and 3 in Table 1. It can be seen that the basic flow structures, including the detonation wave, oblique shock wave, slip line and deflagration surface, are all well captured in Cases 1, 2 and 3, and are qualitatively similar to the published numerical results, e.g. by Schwer et al. [9]. However, finer cellular structures behind the detonation wave and more characteristics induced by instabilities on the slip line and deflagration surface can be captured only by finer grids employed in Cases 2 and 3.

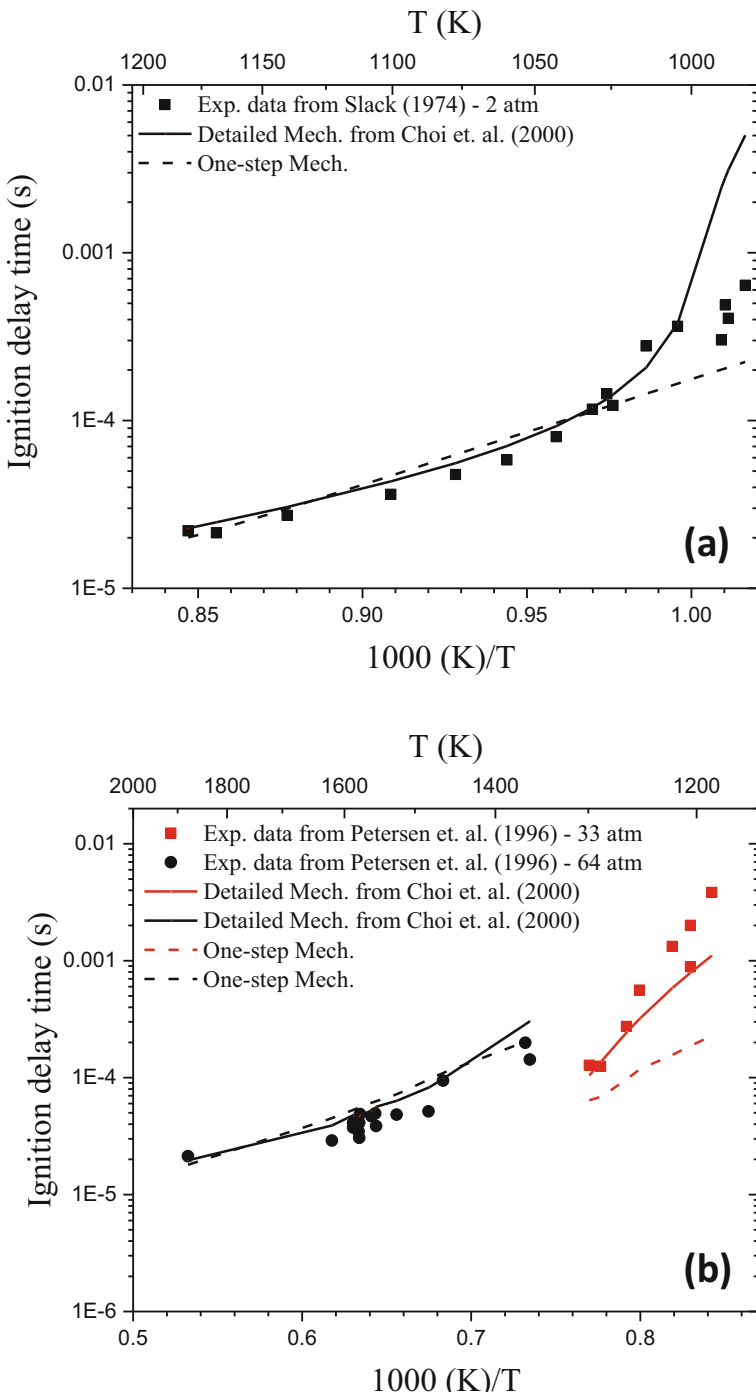


Fig. 2 Ignition delay time from one-step [43] and detailed [44] chemical mechanisms at (a) low (2 atm) and (b) high (33 and 64 atm) pressures. Experimental data in (a) from Ref. [47], while those in (b) from Ref. [48]

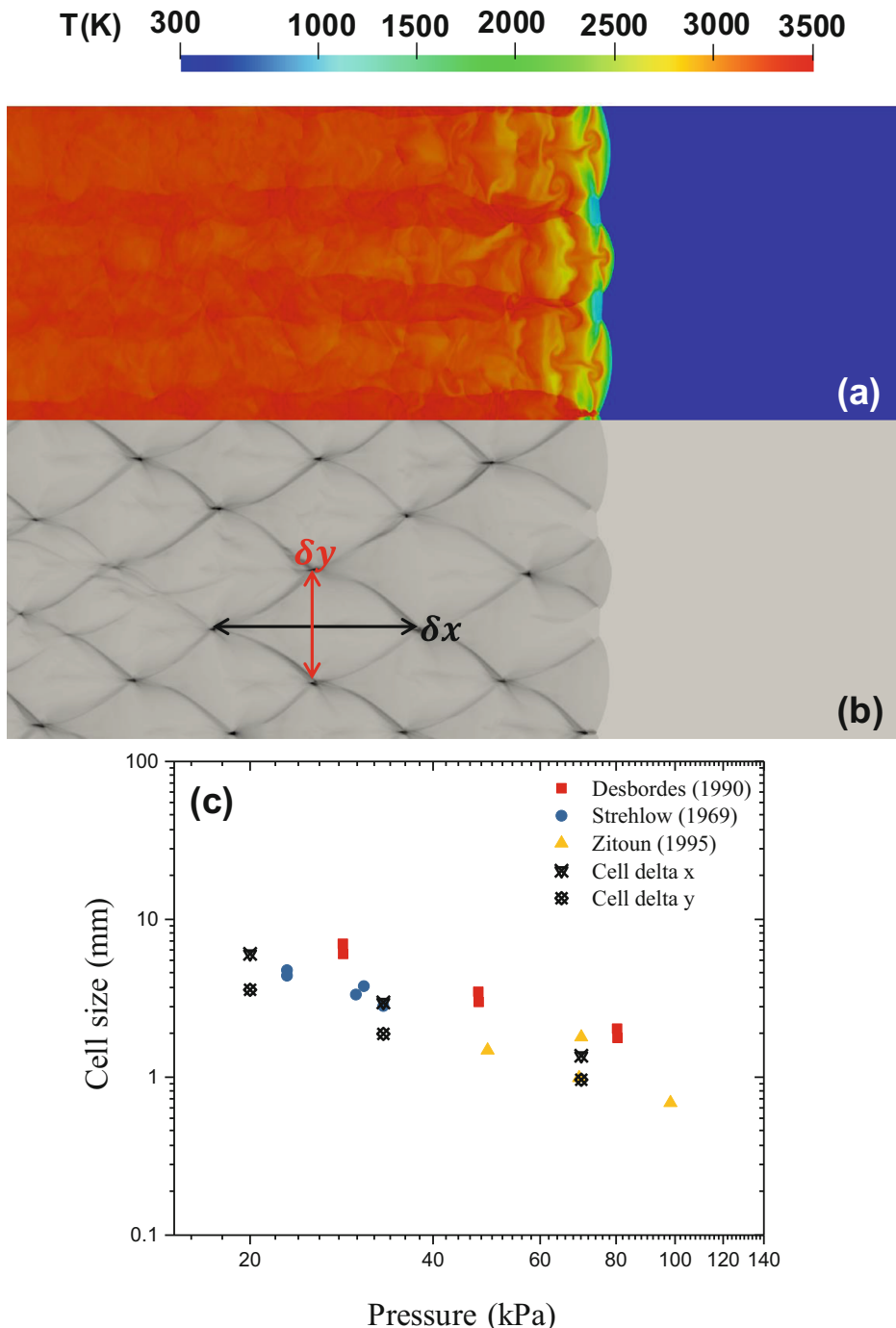


Fig. 3 (a) Temperature, (b) numerical smoked foil and (c) cell width as a function of initial pressure from the one-dimensional detonation tube simulation. Experimental data in (c) are from Desbordes [49] (squares), Engel et al. [50] (circles) and Zitoun et al. [51] (triangles)

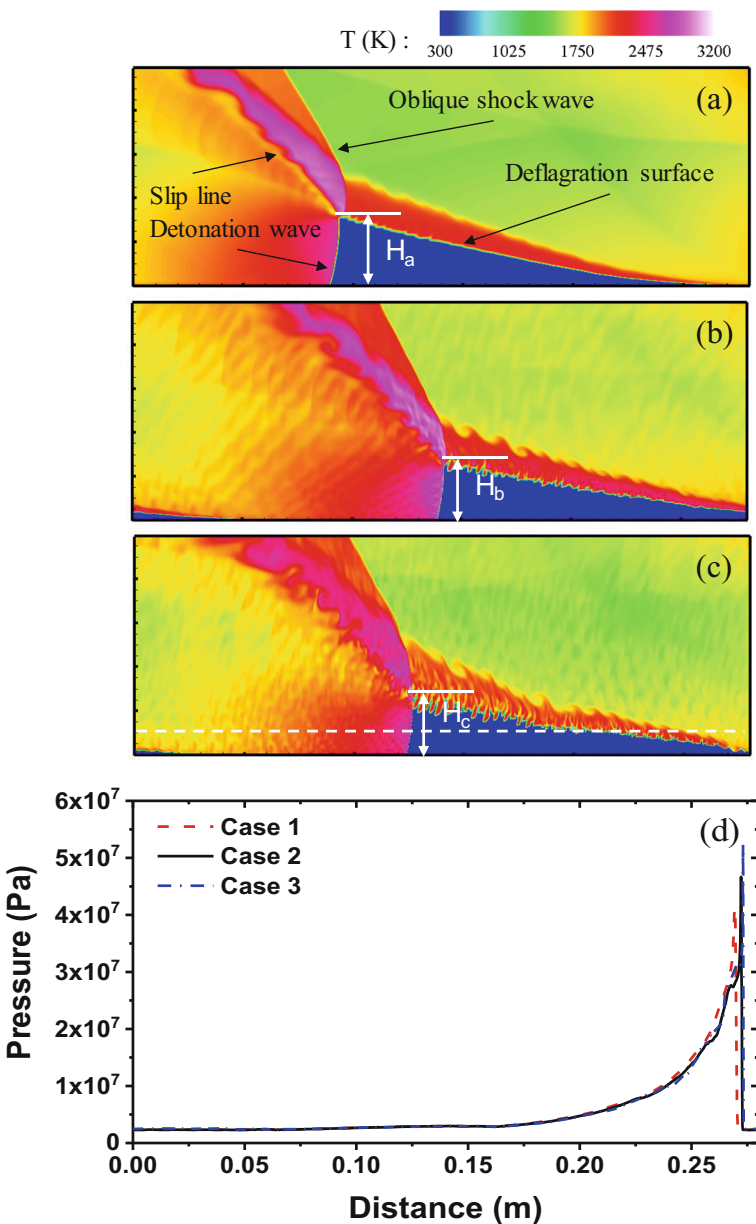


Fig. 4 Distributions of temperature computed with three grids corresponding to Cases (a) 1, (b) 2 and (c) 3, and (d) distributions of pressure along $y = 0.01$ m of RDE. The heights of the detonation front are $H_a = 29.3$ mm, $H_b = 26.0$ mm and $H_c = 25.4$ mm in Cases 1–3, respectively. The white dashed line in (c) indicate the height for pressure profiles in (d). The domain is 280 mm \times 100 mm

In addition, the mean heights of the detonation wave from these three cases are marked in Fig. 4. It should be clarified that the detonation front height H is determined as the maximum y -coordinate, where the heat release rate \dot{Q} is critically less than 10^{13} J/m³/s. The computed propagation speeds are about 1,800 m/s, 1,834 m/s and 1,839 m/s for Cases 1–3, respectively.

From these estimations, one can see that the height and propagation speed of detonation wave of Case 2 are close to those in Case 3 (with relative errors 0.3% and 2.5%, respectively). It can also be found that the height of detonation wave in Case 1 is higher and detonation propagation speed is lower than in Cases 2 and 3. Meanwhile, no qualitative distinctions in terms of combustion dynamics of the detonative and deflagrative waves are observable from Cases 2 and 3 in Fig. 4(b) and (c). If the pressure profiles (at height $y = 0.01$ m, indicated in Fig. 4c) corresponding to a same instant from three cases are compared (see Fig. 4d), we can see that the difference between Case 2 and Case 3 are negligible, which further confirms the above analysis of the temperature contours in Fig. 4(a)-(c). Therefore, based on the current mesh independence analysis, the resolution in Case 2 (see Table 1) will be used in the following simulations.

3.2 Effects of chemical mechanisms

Figure 5 shows the distributions of gas temperature computed with one-step (Case 7) and detailed (Case 2) mechanisms. Main flow structures such as detonation wave, slip line and deflagration surface are all captured with both mechanisms. The computed velocities of detonation wave are also close, i.e. approximately 1,828 and 1,834 m/s respectively. However, there are still some differences between Fig. 5(a) and (b). The higher temperature in the deflagration region in Case 2 indicates stronger combustion there than in Case 7. Unlike the results in Fig. 5(a), the thickness of the deflagration region is finite, which is also observed from the experimental RDE measurements [5, 52]. Due to the fuel consumption along the deflagration surface captured by the detailed mechanism, the height of detonation wave (i.e.

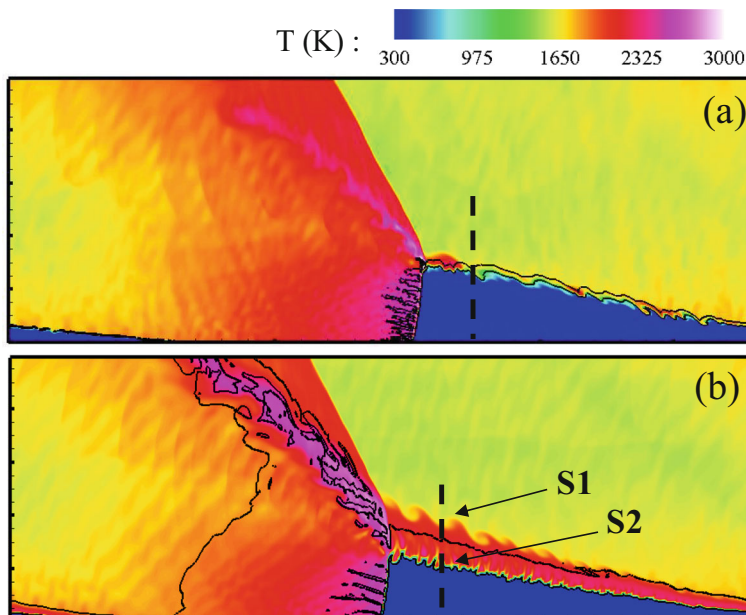


Fig. 5 Distributions of temperature with one-step [43] and detailed [44] chemical mechanisms corresponding to Cases (a) 7 and (b) 2. The solid iso-lines are for heat release rate $\dot{Q} = 10^8$ J/m³/s. The dashed lines in (a) and (b) correspond to the profiles for the results in Fig. 6. S_1 and S_2 are the contact surfaces between fresh gas, deflagration region and burned gas. The domain is 280 mm × 100 mm

about 26 mm) is slightly smaller than that with one-step mechanism (about 31 mm). The slip line begins at the triple point connecting detonation, shock wave and deflagration surface, and its thickness is much larger than that from simulations using one-step chemistry. Similar differences are also present between Cases 4 and 8 ($P_0 = 20$ atm), as well as Cases 5 and 9 ($P_0 = 10$ atm). In general, the above comparisons indicate that the detonation combustion in RDE can be captured by both global and detailed mechanisms [8, 9], while for the deflagration combustion, the one-step mechanism may not suffice.

Figure 6 quantitatively compares key flow parameters across deflagrative reaction layer (dashed lines in Fig. 5) in front of the detonation front predicted with one-step and detailed mechanisms. From simulations with one-step mechanism, the computed heat release rate, temperature, and velocity gradient across the deflagration layer (about $y \approx 0.025$ m) are low compared to the results from the detailed mechanism. For the latter, further analysis should be made here. Noticeably there are two interfaces in the deflagrative layer (see S1 and S2 in Fig. 5b), demarcating the fresh fuel, deflagration and burned gas regions. These two contact surfaces exhibit different unstable characteristics based on the numerical results with detailed chemical mechanisms. The instability along the S1 surface is induced by the Kelvin–Helmholtz (K–H) instability [27, 29], where higher velocity gradient is present but the density difference is negligible. The manifestation of the instability behavior in this surface is the pronounced rolling up of the vortices along S1 which have been demonstrated in Fig. 6(b). The contact surface S2 is experiencing R–T instability, since considerable density difference exists across this surface. This is also observed in the RDE simulations with higher order numerical schemes and detailed mechanisms [27]. It is well-known that R–T instability may happen along an interface of two fluids with different density when the light fluid is accelerated towards the heavy one.

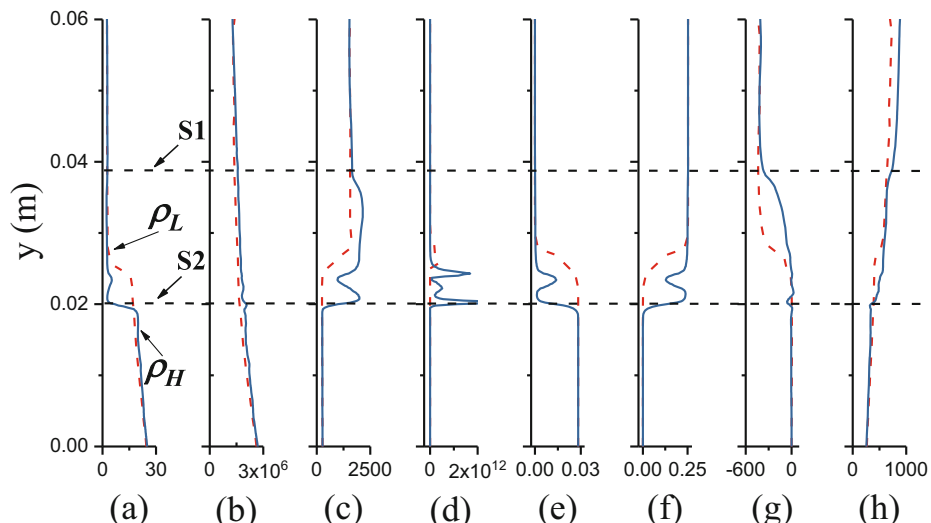


Fig. 6 Flow parameters across the deflagrative layer in front of the detonation (dashed lines in Fig. 5) with one-step (dashed) and detailed (solid lines) mechanisms. The shown variables include: (a) density (kg/m^3), (b) pressure (Pa), (c) temperature (K), (d) heat release rate ($\text{J}/\text{m}^3/\text{s}$), (e) H_2 mass fraction, (f) H_2O mass fraction, (g) velocity component in x -direction (m/s) and (h) velocity component in y -direction (m/s). S1 and S2 are same as in Fig. 5

The Atwood number can be introduced to evaluate the R-T instability [27, 53], which is calculated as

$$At = \frac{\rho_H - \rho_L}{\rho_H + \rho_L}. \quad (7)$$

Here ρ_H and ρ_L denote the density of heavier (fresh gas shown in Fig. 7) and lighter (burned gas) gas at two sides of the interface $S2$, respectively. The density disparity between two fluids induces the R-T instability. When Atwood number At approaches zero, the instability structures are finger-like, while when At is close to unity, they are characterized by the bubble and spike pattern. The Atwood number along the contact surface $S2$ are estimated using Eq. (7) and plotted in Fig. 7(b), and here ρ_H and ρ_L are probed from two immediate sides of $S2$. At stays at a relatively constant value of about 0.8, and therefore the bubble and spike structures are expected to occur at this contact surface [53]. In fact, bubble and spike structures are indeed observed as shown in Fig. 5(b) and more clearly in Fig. 4(c) from a finer grid case.

The R-T instability can be seen as a result of the baroclinic torque, $\nabla\rho \times \nabla p$, created by the misalignment of the pressure and density gradients on the deflagration surface as there exist complex shock waves in an RDE combustor [27]. The baroclinic torque is an important source term in vorticity governing equations, especially for supersonic flows with significant discontinuity like shock waves. Figure 8 shows the magnitude distributions of density gradient ($|\nabla\rho|$), pressure gradient ($|\nabla p|$) and baroclinic term ($|\nabla\rho \times \nabla p|$) calculated from one-step and detailed mechanisms. The flow structures such as detonation wave, oblique wave, transition shock, transverse wave after the detonation and blast wave induced by the K-H instability of the slip line are clearly observed for both

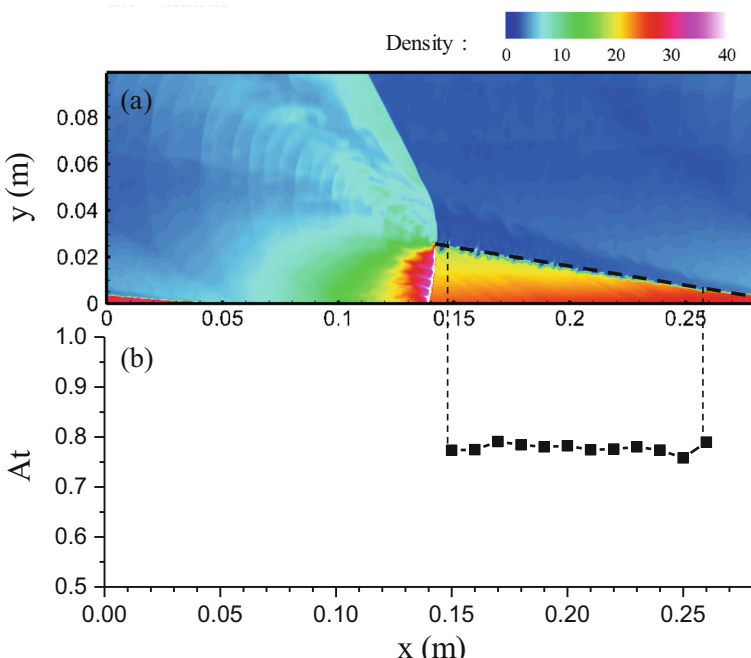


Fig. 7 Distributions of (a) density (in kg/m^3) and (b) Atwood number along contact surface corresponding to the dashed line in (a)

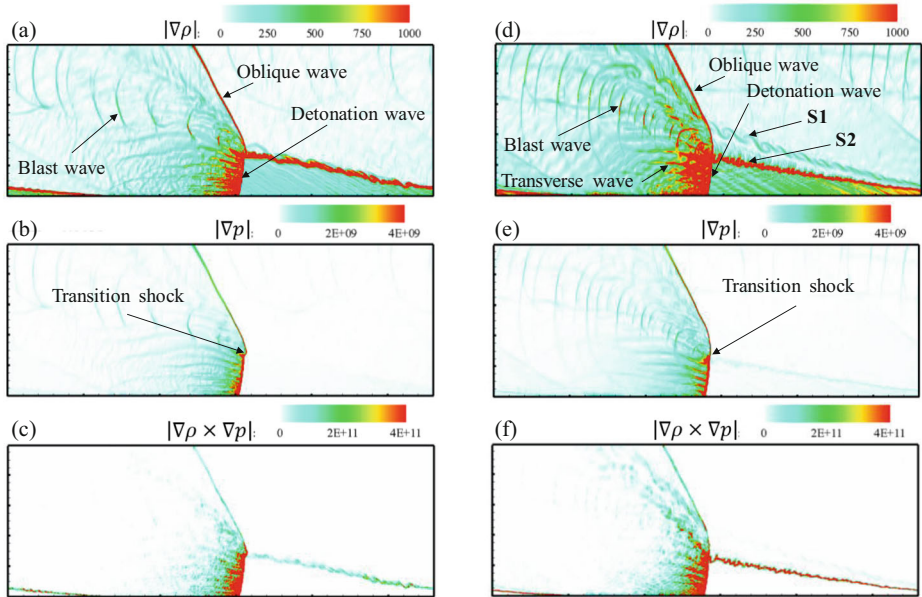


Fig. 8 Contours of magnitudes of density gradient, pressure gradient and baroclinic term with (a-c) one-step and (d-f) detailed chemical mechanisms. The domain is 280 mm × 100 mm. $S1$ and $S2$ are the same as in Fig. 5

scenarios, based on the magnitude of density gradient as indicated in Fig. 8(a) and (d). Note that the blast waves are also seen in the work by Houim and Fievisohn about gaseous layered detonations bounded by an inert gas [54]. Overall, from Fig. 8(b) and (e), the pressure gradients in the deflagration regions in both cases are negligible. However, the magnitudes of baroclinic torque, $|\nabla \rho \times \nabla p|$, along $S2$ (cf. Fig. 8d) are much higher than that along $S1$, as presented from the results with detailed chemistry in Fig. 8(f). This confirms our previous arguments about the occurrence of R-T instability along $S2$.

For the distribution of predicted $|\nabla \rho \times \nabla p|$ with one-step mechanism in Fig. 8(c), it is lower than that along $S2$ in Fig. 8(f). As such, in the detailed mechanism case, this contact surface is characterized by considerable $|\nabla \rho \times \nabla p|$ and pronounced velocity difference (demonstrated in Fig. 6g). One can find that there are small vortices rolling up along this surface, like $S1$ (cf. Fig. 8d). However, no specific structures (like bubble-and-spike structure when $At \rightarrow 1$, or figure-like structure when $At \rightarrow 0$) resulting from R-T instability are generated. Besides the different types of shock waves denoted in Fig. 8(d), we also observe the blast waves obliquely interacting with both $S1$ and $S2$. As such, one can expect that there are some contributions from these shock waves towards increases in $|\nabla \rho \times \nabla p|$ along the interfaces. This may indicate the occurrence of the Richtmyer–Meshkov (R–M) instability. Nevertheless, the blast waves are relatively weak in the results with the one-step chemistry and the similar interactions between the deflagration surface and the blast waves are not observed.

Based on the comparisons made in Figs. 5, 6 and 8, one can see that it is significant to use the detailed chemical mechanism in RDE modelling, if the combustion and flow dynamics along both the detonation and deflagration fronts aim to be predicted accurately. Therefore, the detailed mechanism will be used in the rest of this work to investigate the instability, extinction and re-initiation of rotating detonation in RDE.

3.3 Instability characteristics under constant pressure condition

In the present simulations, effects of the total pressure P_0 on rotating detonation combustion are studied. The cases analyzed in this Sub-section include Cases 2, 4 and 5, which are tabulated in Table 1. Figure 9(a) shows the pressure history (spanning for 0.007 s, corresponding to 45 cycles or so) at one probing location close to the head end with different total pressures, i.e. $P_0 = 10, 20$ and 40 atm, while the time series for $t = 0.005\text{--}0.006$ s are plotted in Fig. 9(b). The results show that variations of the total pressure have negligible effects on the propagation speed of the detonation wave (about 1,830 m/s) in the RDE combustor. Meanwhile, the detonation rotation frequency is about 6,400 Hz from all the three cases. However, the peak pressure when the detonation front crosses increases with the increased P_0 . Specifically, the maximum pressures for $P_0 = 10, 20$ and 40 atm are as high as approximately 100, 200 and 600 atm, respectively. Note that the peak pressures at three pressure, e.g. 600 atm at $P_0 = 40$ atm, are close to their von Neumann pressures computed from The Shock & Detonation Toolbox [42].

Figure 10 shows the time evolutions of density gradient for $P_0 = 10, 20$ and 40 atm. The results in Fig. 10(a₁)–(a₆) with $P_0 = 10$ atm show that the contact surface becomes highly

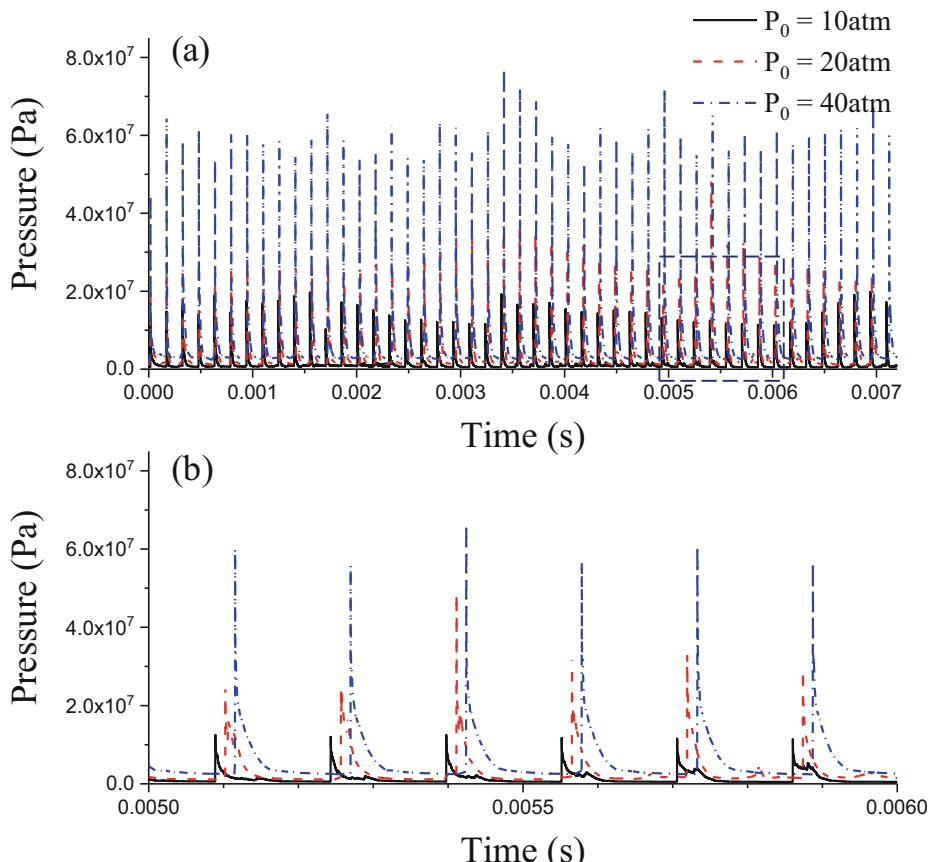


Fig. 9 Pressure history from one probe location close to the head end with detailed chemical mechanism

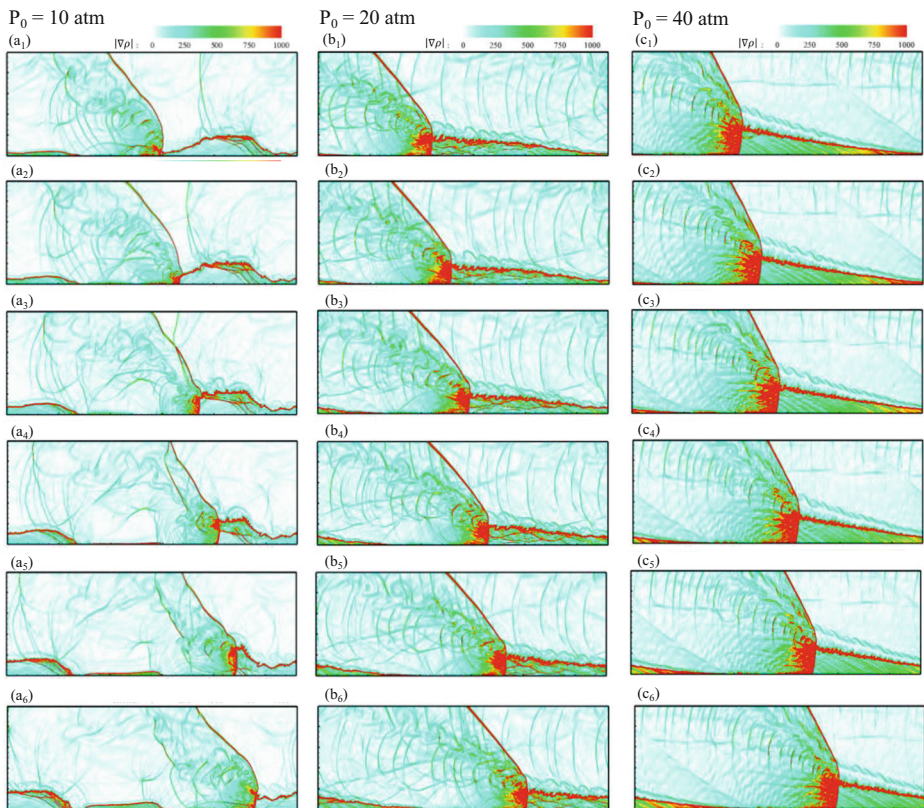


Fig. 10 Time evolution of density gradient for different total pressures: **(a)** $P_0 = 10$ atm, **(b)** $P_0 = 20$ atm and **(c)** $P_0 = 40$ atm. The domain is 280 mm × 100 mm. Row 1 to Row 6 represent 0.003 s – 0.00305 s, with equal time interval 0.00001 s

distorted and wrinkled and experiences strong instability, which may lead to destabilization of the detonation front and slip line in the RDE chamber. This instability is induced by the comparatively high pressure and reflected shock wave after the detonation wave [28]. Note that although the rotating detonation combustion is not stable in this case, nevertheless, it is not quenched. For $P_0 = 20$ atm in Fig. 10(b₁)–(b₆), interactions between the contact surface and blast wave induced by the K–H instability of the slip line induce some shock waves in the fresh premixed H₂–air region. The influences of these shock waves on the inflow boundary would lead to the instability of the local mass flow rates at the head end of the RDE chamber. The contact surface ultimately becomes unstable (not shown in Fig. 10), which is similar to the results with $P_0 = 10$ atm. However, this instability occurs later than that with $P_0 = 10$ atm. Different from $P_0 = 10$ and 20 atm, with $P_0 = 40$ atm, the rotating detonation combustion is more stable, based on Fig. 10(c₁)–(c₆), and no pronounced distortion and wrinkling of the contact surface arise for the entire shown physical time (we compute for a longer time, and find that no destabilization occurs). This is due to the high compression in the fresh mixture with higher total pressure so that the fuel mass rates are not greatly be affected from the downstream perturbations associated with the detonation and deflagration in the RDE chamber. Moreover, for cases $P_0 = 10$ atm, 20 atm and 40 atm, the pressure ratios defined as the ratio of total pressure at the outlet and inlet are about 1.57, 1.78 and 1.8, respectively. For the case of $P_0 =$

10 atm in the present simulations, the unstable detonation wave is observed, which means that the unstable detonation wave may reduce the performance of an RDE combustor.

Based on Figs. 9 and 10, even if the deflagrative front is unstable, one can still obtain the stable pressure time series. It is well-known that the pressure-time trace in RDE can indicate significant and direct information about detonation operational stability [15, 22, 24]. Nevertheless, for unstable deflagration fronts in RDE burner, it is not straightforward to obtain the similar information through the pressure history due to their constant-pressure combustion characteristics. Therefore, if the RDE experimentalists or modelers would like to know the detailed and transient information about the dynamics of these two fronts, use of more data acquisition approaches, like OH-PLIF and OH* chemiluminescence [5, 52, 55], may be made to visualize the internal field for comprehensive analysis.

The time series of mass flow rate ($\dot{m}_R = \int_A \rho u dA$), thrust force at outlet plane ($F = \int_A [\rho u^2 + (p - p_b)] dA$), specific impulse ($I_{sp} = F/g\dot{m}_R Y_{H2}^0$), and detonation front height H for different total pressures are respectively shown in Fig. 11(a) – (d). Here g is gravity acceleration, Y_{H2}^0 is the hydrogen mass fraction in the stoichiometric H₂-air mixture injected into the RDE and p_b is the backpressure. Three total pressures are shown here, i.e. $P_0 = 10, 20. It can be observed from Fig. 11(b) and (c) that although mass flow rate \dot{m}_R and thrust force F change with total pressure P_0 , however, the three cases predict almost the same averaged specific impulse as shown in Fig. 11(a). The specific impulse, mass flow rate and force at outlet plane of lower P_0 (i.e. 10 and 20 atm) become unstable, characterized by the high-frequency, low-magnitude and periodic oscillations in the respective time series. These are consistent with the results in Fig. 10. Meanwhile, the time for onset of destabilization increases with total pressure P_0 . Specifically, for $P_0 = 10, it is around 0.0013 s, while for $P_0 = 20\text{ atm}$, it is about 0.003 s. This implies that to evaluate the RDE operational performance from computations and/or experiments, the sampling time should be sufficiently long with enough cycles.$$

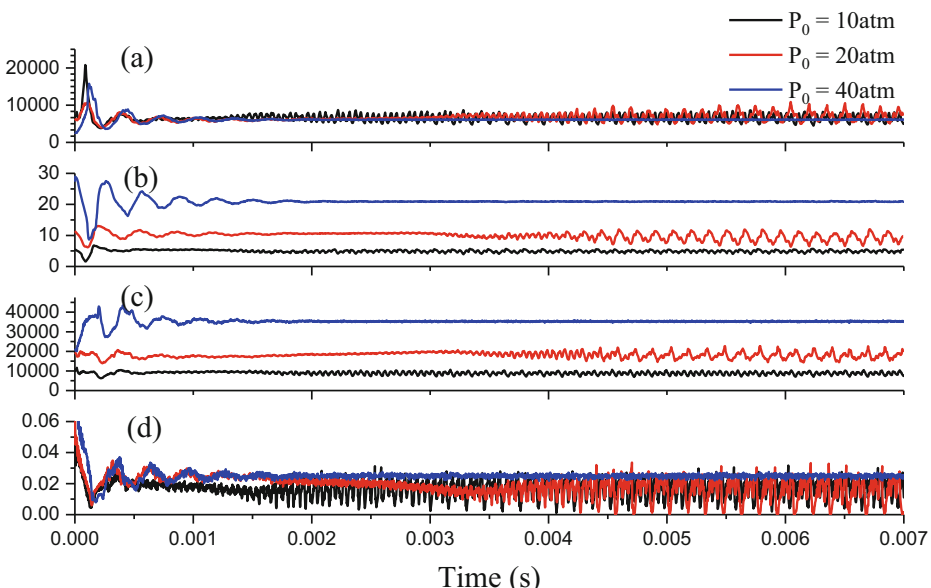


Fig. 11 Time history of (a) specific impulse (s), (b) mass flow rate (kg/s), (c) thrust force at the outlet plane (N) and (d) height of detonation front (m) for different total pressures

Moreover, overall performance is stable for $P_0 = 40$ atm. Thus, similar features are observed from Fig. 11(d) for the detonation height. Once the unstable combustion occurs in the RDE chamber, the height fluctuates periodically. Particularly, for $P_0 = 20$ atm, it is reduced to almost zero, but can increase sharply to a finite value. The variations of the detonation front height are essentially affected by the destabilization of the deflagrative surfaces as discussed in Fig. 10.

Fast Fourier transform (FFT) analysis is performed in Fig. 12 for the time history of specific impulse I_{sp} , which are shown in Fig. 11(a). The current FFT analysis is based on the time series in which the initial transition effects are excluded. For unstable cases ($P_0 = 10$ and 20 atm) in Fig. 13(a) and (b), the frequency of the instability is about 20,000 Hz. However, no dominant frequency is observed for stable case $P_0 = 40$ atm in Fig. 12(c). It should be mentioned that the same frequency is also obtained (about 20,000 Hz) for the above two unstable cases simulated with same P_0 conditions and one-step chemistry (results not shown here). This dominant frequency may be intrinsically related to RDE geometrical configurations and/or fuel compositions. Therefore, for designing practical RDE burners and selecting the proper fuels, the global combustion stability may need to be comprehensively accessed. Note that the combustion instability phenomena discussed in this Sub-section result from the intrinsic interactions between the shock waves, deflagration and detonation fronts. In the following, the instability characteristics due to the forced total pressure oscillations will be discussed.

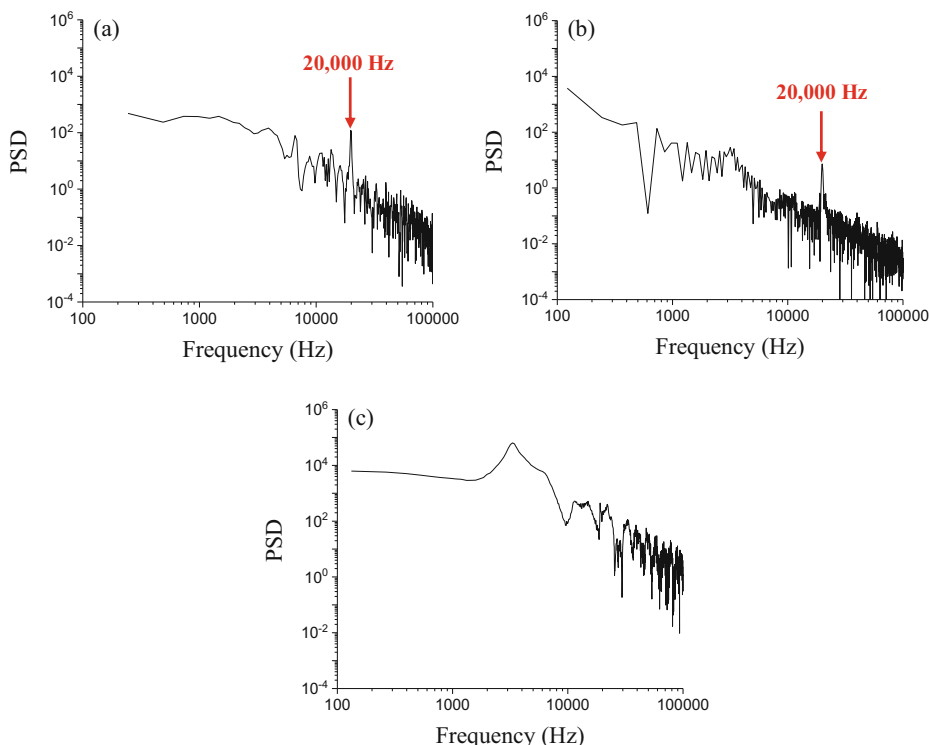


Fig. 12 Power spectrum density of specific impulse time series for different total pressures: (a) $P_0 = 10$ atm, (b) $P_0 = 20$ atm and (c) $P_0 = 40$ atm

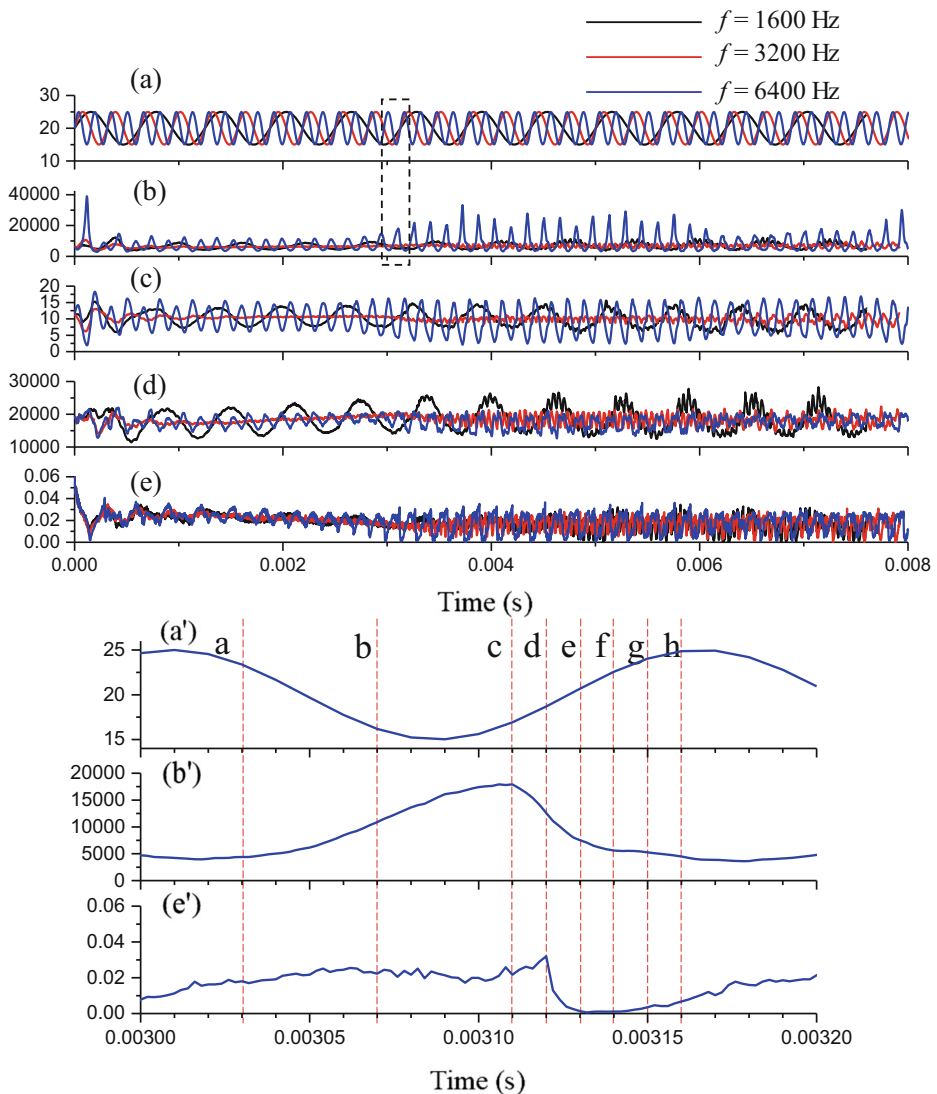


Fig. 13 Time history of (a) total pressure, (b) specific impulse, (c) mass flow rate, (d) thrust force at the outlet plane and (e) height of detonation with time-varying total pressures. Time history of (a') total pressure, (b') specific impulse and (e') total pressure within one period as indicated with dashed box in (a) and (b)

3.4 Instability characteristics under time-varying pressure condition

Simulations with time-varying total pressures are next performed to investigate their influences on dynamics of detonation and deflagration fronts and the global RDE performance. The information on the simulated cases, i.e. Cases 10, 11 and 12, has been listed in Table 1. The variations of the total pressures are given in Eq. (6), and the external frequencies f in Cases 10, 11 and 12 are 6,400, 3,200 and 1,600 Hz, respectively. As mentioned in Sub-section 2.4, $f=6,400$ Hz is roughly equal to the rotating frequency f_0 obtained from the constant P_0 cases in Cases 1–9. As mentioned in Sub-section 2.4, this value is selected to mimic the forced

perturbations with high frequencies from the propellant plenum in practical RDE system. Figure 13(a)-(e) present the time series of total pressure, specific impulse, mass flow rate, force at the exit plane and height of detonation wave for three total pressure conditions. The results from Fig. 13(b) and (c) show that, for the specified frequency with $f=3,200$ Hz, the influences of variable total pressure on the specific impulse and fuel mass flow rate are the smallest. For the case with $f=6,400$ Hz, the magnitudes of the specific and fuel mass flow rate are the strongest. About the propulsive force at the exit plane, the largest magnitude is from the forced frequency $f=6,400$ Hz. Also, strong fluctuations can be observed from all the three cases in Fig. 13(e). In general, it can be seen that the changes of the specific impulse, inlet mass flow rate, force at outlet plane and height of detonation depend on the forced frequency for the total pressure.

To quantify the frequencies from the three cases, results of the FFT analysis of the specific impulse for them (correspond to Fig. 13b) are respectively shown in Fig. 14(a)-(c). Similar to the procedure in Fig. 12, FFT analysis in Fig. 14 is performed based on the time series without initial effects. Multiple characteristic frequencies are identified in each situation. The frequency $f_0=20,000$ Hz is captured for all the cases. Besides the forced frequency ($f=6,400$ Hz in Fig. 14a, 3,200 Hz in Fig. 14b and 1,600 Hz in Fig. 14c), three harmonic frequencies can also be observed, i.e. $2f$, $4f$ and $6f$, as marked in Fig. 14. The dominant frequency is affected by the forced external input. One can see that, based on the current computational results, the dominant frequency is either the forced frequency (for $f=6,400$ Hz and 1,600 Hz) or the intrinsic frequency $f_0=20,000$ Hz (for $f=3,200$ Hz). Levin et al. numerically studied the pressure variations in the RDE chamber when the inlet total pressure linearly changes [34]. However, in his work, no dominant frequency is reported.

Figure 13(a'), (b') and (e') show the time series of total pressure, specific impulse and detonation front height in one period of the pressure variation. In this duration, the specific impulse and detonation height show the significant changes. To visualize the corresponding transients, Fig. 15 shows the temperature distributions at several instants as indicated in Fig. 13(a'), (b') and (e'). Continuously rotating detonation combustion always exists, but relatively regular triangular fresh fuel mixture region (typically exist in stable RDE combustion, e.g. like in Fig. 4) disappears due to the highly distorted deflagrative surfaces. In fact, this distortion of the fresh fuel mixture region is also observed in the unstable cases with constant total pressure (see Fig. 10), but is worse in Fig. 15. In addition, the height of the detonation front H is reduced from about 0.03 m to 0 for this period. When the height is zero, the shock wave and combustion separation (see in Fig. 15e) and ephemeral quenching of detonation occurs (see in Fig. 15f). From Fig. 13(a'), it can be seen that P_0 is increasing when H is zero at $t=0.00314$ s. Detonation re-initiation close to the head end of the RDE chamber (marked in Fig. 15g) can be clearly seen at $t=0.00315$ s in Fig. 15(g). This is caused by the new availability of the fresh fuel mixture near the previously detonated gas zones (with temperature greater than 2,800 K). However, it should be noted that the presence of shock wave and combustion separation, quenching of detonation and re-detonation are detrimental for the RDE combustion efficiency [1, 2].

3.5 Extinction and re-initiation under extreme pressure condition

The extinction and re-initiation of rotating detonative combustion under extreme pressure conditions (e.g. in practical RDEs, the sudden change of the total pressure in the upstream plenum, possibly related to the variations of the fuel flow rate) will be discussed in this Sub-

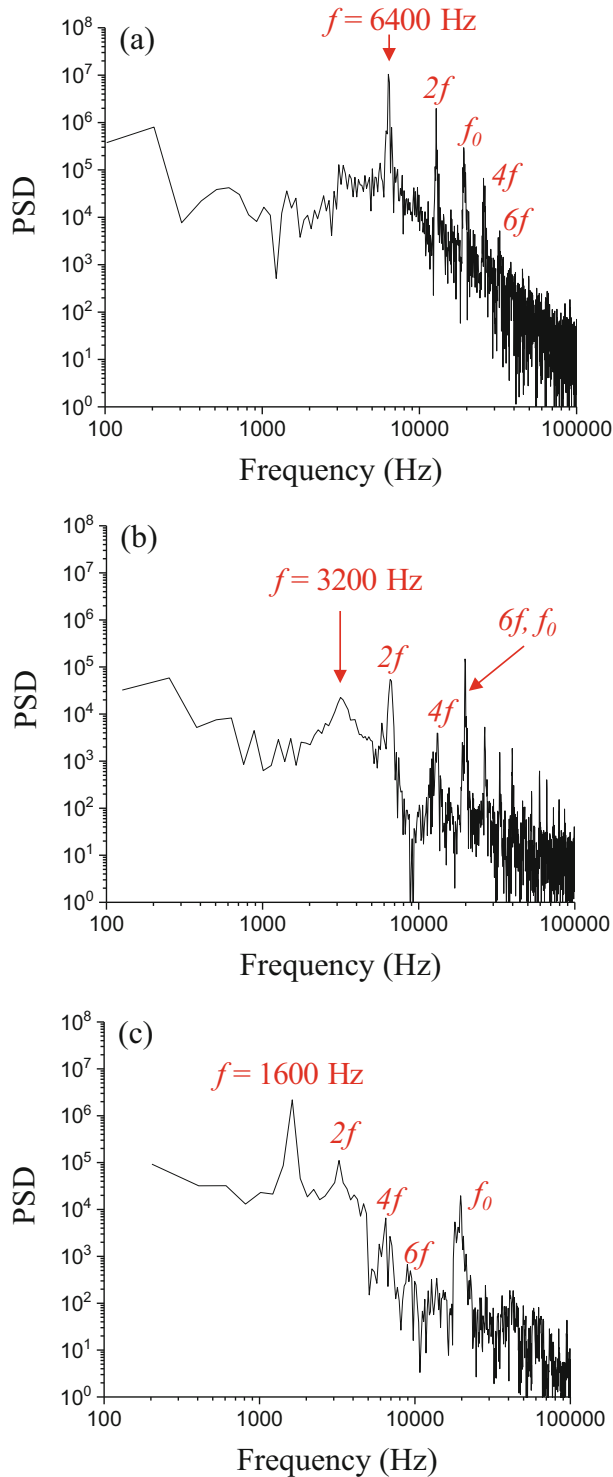


Fig. 14 Power spectrum density of specific impulse time series for time-varying inflow total pressures

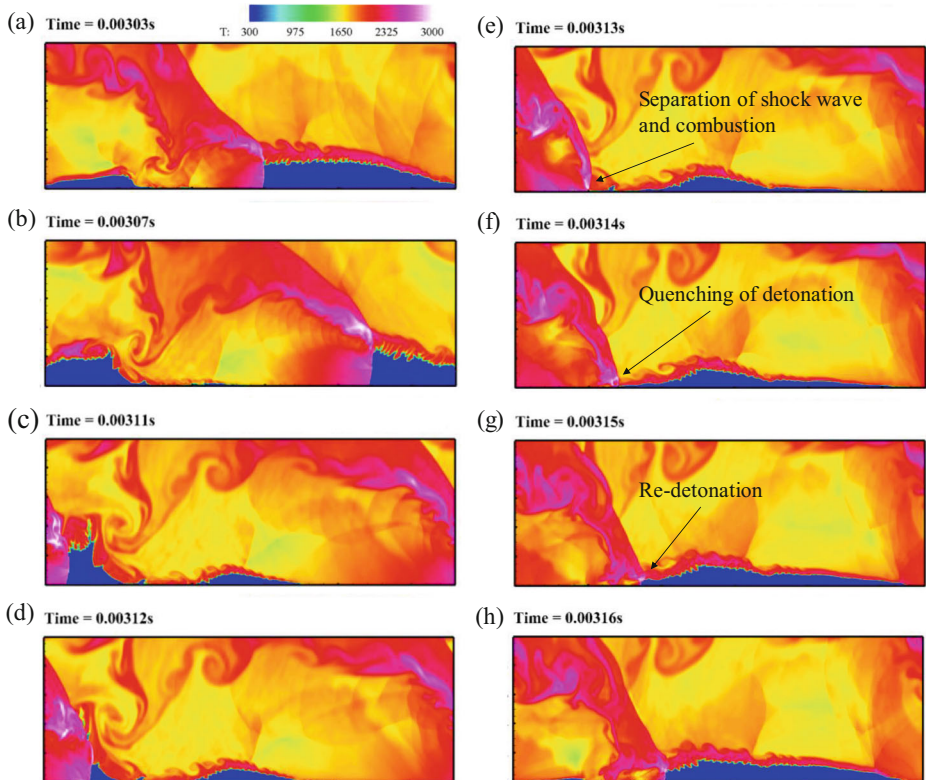


Fig. 15 Time evolution of temperature within one period as shown in Fig. 13(a'). The time for (a)–(h) is marked with dashed lines in Fig. 13(a'). The domain is 280 mm × 100 mm

section. For the sake of simplicity and without loss of the generality, two scenarios are investigated, i.e. one with sudden drop of the total pressure P_0 in a stably run RDE, whilst the other with sudden increase of P_0 from a just extinguished field.

Figure 16(a)–(d) respectively shows the time series of specific impulse I_{sp} , thrust force F at exit plane, mass flow rate \dot{m}_R and height H of detonation front for the first scenario. The initial field is from a stably rotating detonation combustion with $P_0 = 10$ atm (corresponding to the initially stable results from Case 5) and the total pressure P_0 is artificially reduced to 5 atm through modifying P_0 at the boundary condition. The mass flow rate/specific impulse decreases/increases abruptly due to the change of P_0 . Particularly, at around $t = 0.0003$ s, no fuel is injected into the RDE chamber due to relatively low P_0 enforced in this case. The specific impulse is mainly affected by the mass flow rate, and therefore it considerably increases close to $t = 0.0003$ s due to $\dot{m}_R = 0$. Conversely, based on Fig. 16(b), the thrust force at the exit plane stays unchanged for the initial 0.00007 s and then decreases gradually. The height of the detonation front firstly decreases gradually, then fluctuates irregularly and eventually becomes zero at $t = 0.00023$ s, indicating the ultimate quenching of the rotating detonation. Levin et al. also observed the extinction of the detonation through numerical simulations when the total pressure is continuously reduced and they mention the existence of the minimal total pressure, below which the rotating detonation wave cannot sustain itself [34].

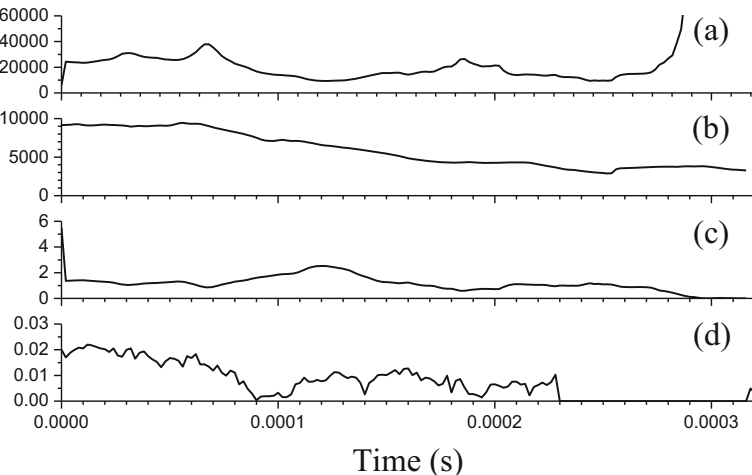


Fig. 16 Time history of (a) specific impulse (s), (b) thrust force at the outlet plane (N), (c) mass flow rate (kg/s) and (d) height of detonation front (m) for decreasing total pressure to 5 atm from a RDE field with 10 atm

Plotted in Fig. 17 are the distributions of temperature fields corresponding to the case in Fig. 16 and the durations span from $t = 0$ to 0.0003 s. The pressures between the downstream and upstream of the contact surface are not balanced due to the suddenly changed P_0 and hence the local flow downstream begins to influence the contact surface. It can be seen that the oblique shock wave and contact surface are distorted (see Fig. 17c and d). This further leads to the deformation and thickening of the slip line behind the detonation front (Fig. 17d), which in turn affects the contact surface, the flow in the fresh pre-mixture zone and also mass flow rate at the inlet (Fig. 17d and e). The results of Fig. 17(c) and (d) show that although the mass flow rate becomes zero at 0.00029 s, the quenching of detonation wave begins earlier, i.e. at 0.00023 s corresponding to Fig. 17(g), when the separation of shock wave and combustion can be clearly observed. The detonation wave is finally quenched, if there are no sufficient mixture injected into the RDE combustor under the long-lasting lower pressure condition.

Corresponding to the second scenario, re-initiation of the rotating detonation is also investigated, through increasing P_0 based on an initial field in which the rotating detonation is just quenched (corresponding to the results in Fig. 17j, i.e. $t = 0.0003$ s). Figure 18 shows the time history of specific impulse I_{sp} , thrust force F at exit plane, mass flow rate \dot{m}_R and height H of detonation front after P_0 is increased from 5 atm to 40 atm in the boundary condition. The mass flow rate \dot{m}_R first increases intermediately and then stays close to a constant value. However, for the specific impulse and thrust force, their respective response to the pressure change is delayed around 0.00006 s and afterwards slow increase occurs. One can find that the detonation wave is formed, almost instantly after P_0 is altered. This can be loosely quantified through the increases of the detonation front height H in Fig. 18(d).

Figure 19 demonstrates the unsteady re-initiation process of the rotating detonation combustion with the time evolutions of instantaneous temperature, pressure and the heat release rate in the RDE chamber. Figure 19(a) shows the initial distributions of temperature and pressure, i.e. a fully quenched detonation in the RDE. However, after 4×10^{-6} s, a thin layer (blue region in Fig. 19b) of fresh pre-mixture appears near the top head of the chamber. Intense deflagrative combustion can be found along some sections of the interface between this layer and the product gas. At $t = 8 \times 10^{-6}$ s, very localized high pressure (more than 40 atm) and high

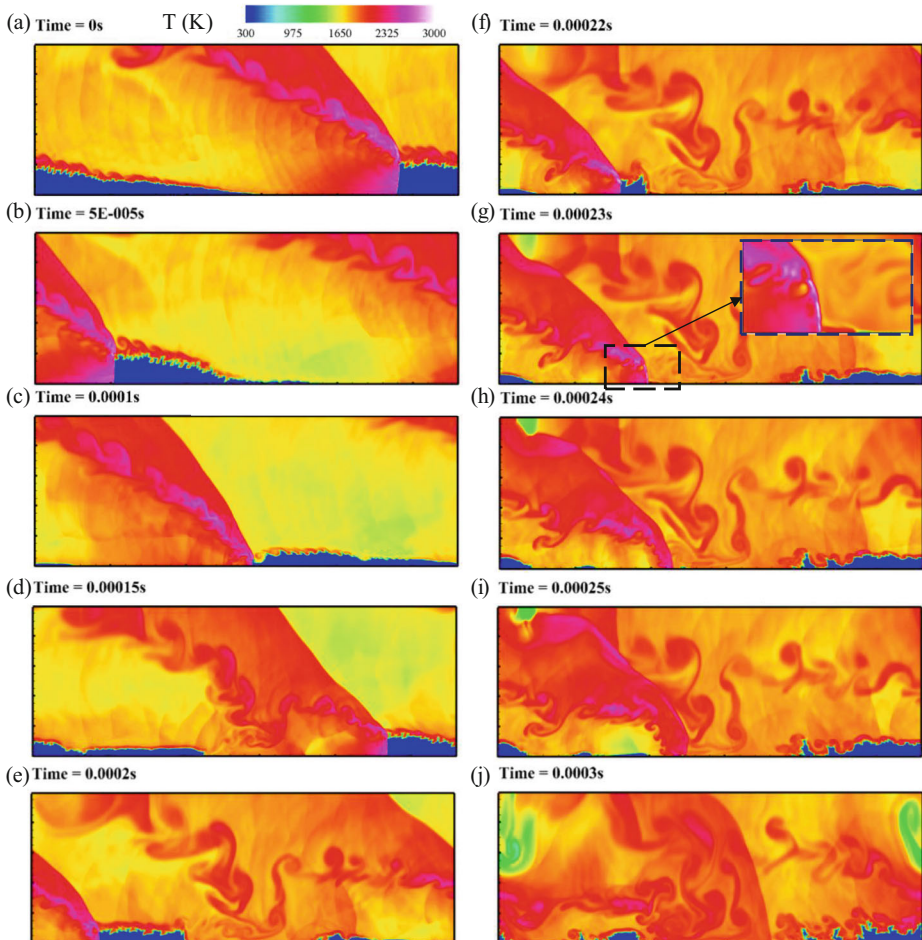


Fig. 17 Time evolutions of temperature for decreasing total pressure to 5 atm from a RDE field with 10 atm. The domain is 280 mm × 100 mm

heat release rate occur at some locations along the interface (see the enlarged region in right figures in Fig. 19c). This implies that initial detonation is formed in these regions. However, the temperature there (about 2,400 K) is not as high as the temperature (about 2,900 K) in the re-initiation process discussed in Fig. 15, in which the re-initiation is due to the higher local temperature and re-filling of the fresh fuel pre-mixture. Re-initiation of the detonation fronts in such conditions can be attributed to the local high pressure.

In reality, based on the results in Fig. 19(d) – (f), multiple small detonation pockets are developed concurrently, e.g. D1, D2 and D3, due to the local favorable conditions (i.e. relatively high pressure). At these instants, the recharged fuel mixtures have become more abundant compared to $t=4 \times 10^{-6}$ s. Due to the non-uniform pressure distributions alongside the detonation front, the front would preferentially propagate towards the fresh fuel layer. For instance, D1 and D3 move towards the left side, whilst D2 towards the right side, as indicated by the arrows in Fig. 19(f). Based on the transient results (not shown in Fig. 19), D2 and D3 collide with each other after

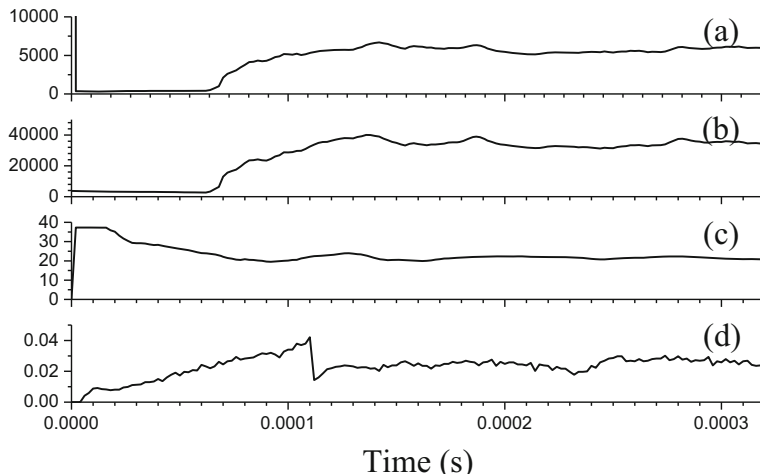


Fig. 18 Time history of (a) specific impulse (s), (b) thrust force at the outlet plane (N), (c) mass flow rate (kg/s) and (d) height of detonation front (m) for increasing total pressure to 40 atm from a quenched RDE field

they start their respective propagation, and D2 is weakened gradually and finally quenched. D3 survives from this collision and continue moving towards left side, resulting in two co-propagating detonation fronts, i.e. D1 and D3. After about one cycle for propagation, D1 is also degraded due to less fuel in front of it and finally only one stable detonation wave D3 can continuously propagate towards left side, which is not shown in Fig. 19.

The qualitatively similar detonation re-initiation phenomena (i.e. high-pressure induced detonation wavelets, subsequent collisions and final stable propagation) are also observed by Yao et al. through their three-dimensional simulations of RDE burner with one-step chemistry [56]. However, the underlying mechanisms are not the same. They attributed it to the chamber wall compression, whereas in our case the localized high-pressure region is generated due to increased pressure in the refilling layer. In addition, the re-initiation in RDE due to increased total pressure is also experimentally observed by Ma et al. in their RDE burner with fuel/air partial premixing through the pressure history [57]. Our foregoing simulation results may provide the hints to explain this complicated phenomenon.

Two comments should be made here about RDE re-initiation. Firstly, based on our other tests not presented here, we find that it is of great importance to select the proper initial fields to achieve the successful initiation of the rotating detonative combustion. The detonation re-initiation becomes more difficult around 0.0002 s after extinction from the simulations here, since after 0.0002 s localized high-pressure region does not arise any more from the deflagration-dominated field. Secondly, re-initiation stochasticity can be observed, in terms of the location and number of initial detonation front, the propagation direction, their interaction and final stabilization. It may be related to the local characteristics of the flow field, e.g. pressure and upstream boundary conditions. The stochasticity is also highlighted by St George et al. for their experimental investigations on onset of the rotating detonation combustion [58]. To draw more general conclusions on this highly transient process, further numerical and experimental investigations may be needed.

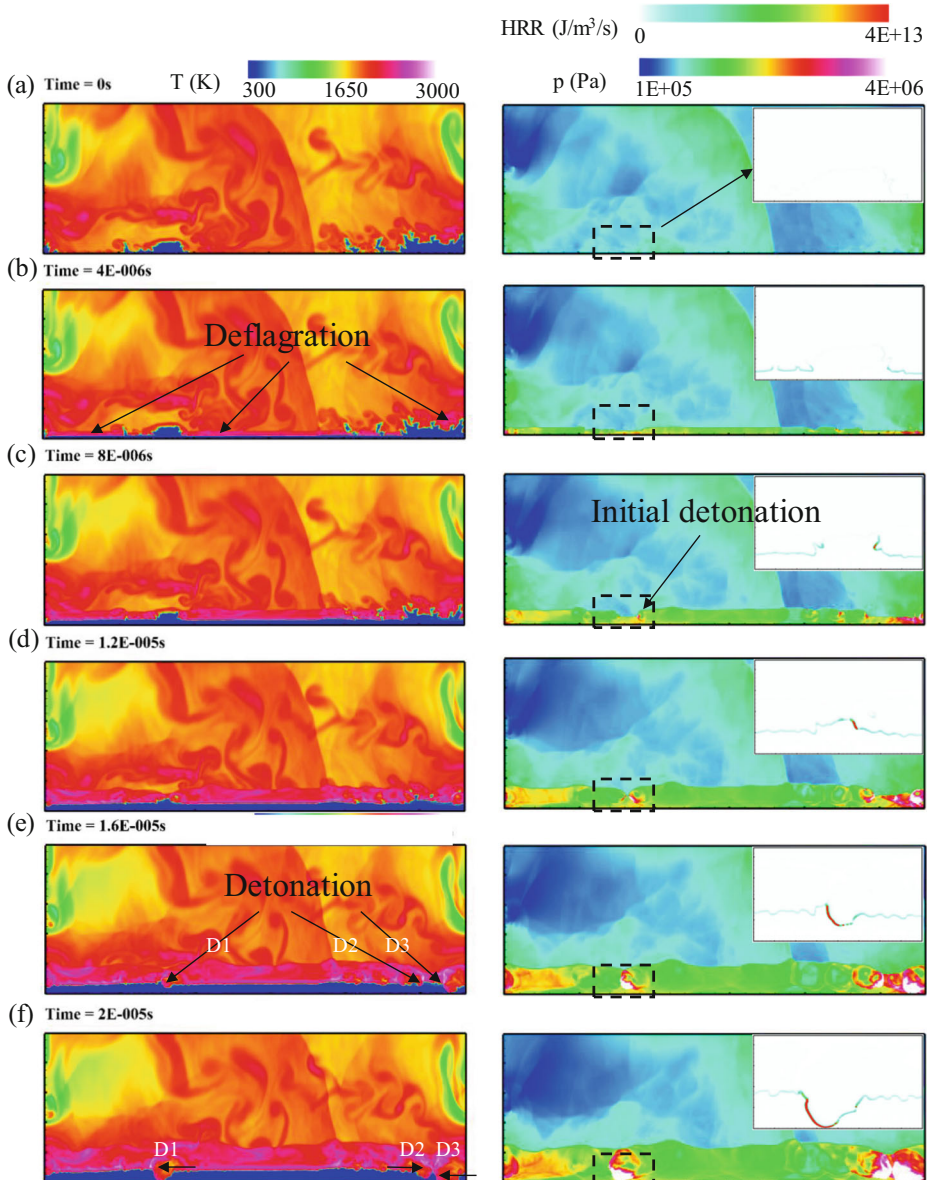


Fig. 19 Time evolutions of temperature (left), pressure (right) and heat release rate (inset) for increasing total pressure to 40 atm from a quenched RDE field. Arrows in (f) denote the propagation directions of the three detonation pockets, i.e. D1, D2 and D3. The domain is 280 mm × 100 mm

4 Conclusions

Instability, extinction and re-initiation of rotating detonation combustion in a two-dimensional RDE configuration are numerically investigated, and the emphasis is laid on the effects of variable total pressure on the above combustion dynamics, to mimic the pressure perturbations from the upstream of fuel plenum in RDE system. The global and detailed chemical

mechanisms are used and the results demonstrate that although both can capture the characteristics of rotating detonation, however, the predictions of deflagrative surface with detailed chemistry are qualitatively closer to the experimental observations.

About combustion instability in RDE, two conditions, i.e. different constant pressures and time-varying (sinusoidal) pressures, are considered. The results show that under constant pressures the rotating detonation combustion is more likely to de-stabilize at low total pressure, due to the onset of the instability from the deflagrative surface. The intrinsic frequency for the unstable cases with different constant pressures are close and may be caused by the RDE configuration and/or fuel properties. For the time-varying pressures with various specified frequencies in the sinusoidal signals, the RDE shows the different levels of the instability are characterized by multiple frequencies. The dominant frequencies under time-varying total pressure depend on the competition between the forced external frequency and also the intrinsic one from the RDE system.

To investigate extinction and re-initiation of continuously rotating detonation, the total pressure is artificially changed abruptly at the fuel inlet boundary condition. It can be found that the detonation is quenched (characterized by the decoupling of the shock and reaction front), with only deflagrative combustion active, when the total pressure is reduced to a relatively lower value. Accordingly, the overall performance (e.g. specific impulse and thrust force) of the RDE deteriorates. Also, when the total pressure is increased based on the just quenched flow fields, the detonation wavelets are initiated due to the localized high pressure along the fuel/air contact surface. The stochasticity in RDE re-initiation has been found, in terms of the location and number of initial detonation front, the propagation direction, their interaction and final stabilization.

We do not consider the reactant injector system and fuel/air mixing in the current work. In practical RDE combustors, separate fuel injection systems are always used. However, the observations from the current work which considers the premixed RDE configuration are still useful. Essentially, detonation is a premixed combustion phenomenon, and studies on premixed reactants can help us exclude the fuel/oxidizer mixing effects on detonation and then focus on the specific RDE combustion dynamics (e.g. instability and extinction). Also, due to the high-speed flows and strong turbulence in the practical RDE chamber, the separately injected mixture immediately downstream of the chamber top end (where the detonation fronts exist) tends to be partially premixed. In our future work, numerical simulations on RDE with separate fuel/oxidizer injection will be conducted to further investigate the critical combustion dynamics.

Acknowledgements The numerical simulations were performed with the computational resources from National Supercomputing Center (NSCC), Singapore (<https://www.nscc.sg>). The authors thank the anonymous reviewers for their useful comments to improve the manuscript.

Compliance with Ethical Standards

Conflict of Interests The authors declare that they have no conflict of interest.

References

1. Zhou, R., Wu, D., Wang, J.: Progress of continuously rotating detonation engines. Chinese J. Aeronaut. **29**, 15–29 (2016)
2. Kailasanath, K.: Recent Developments in the Research on Rotating-Detonation-Wave Engines. In: 55th AIAA Aerospace Sciences Meeting. American Institute of Aeronautics and Astronautics (2017)

3. Lu, F.K., Braun, E.M.: Rotating detonation wave propulsion: experimental challenges, modeling, and engine concepts. *J. Propuls. Power.* **4**, 464–470 (2014)
4. Schwer, D., Kailasanath, K.: Fluid dynamics of rotating detonation engines with hydrogen and hydrocarbon fuels. *Proc. Combust. Inst.* **34**, 1991–1998 (2013)
5. Rankin, B.A., Richardson, D.R., Caswell, A.W., Naples, A.G., Hoke, J.L., Schauer, F.R.: Chemiluminescence imaging of an optically accessible non-premixed rotating detonation engine. *Combust. Flame.* **176**, 12–22 (2017)
6. Codoni, J.R., Cho, K.Y., Hoke, J.L., Rankin, B.A., Schauer, F.R.: Simultaneous mid-IR H_2O/CO_2 emission and OH chemiluminescence measurements within a RDE operating with and without backpressure. 2018 AIAA Aerosp. Sci. Meet. 1–13 (2018)
7. Sun, J., Zhou, J., Liu, S., Lin, Z., Cai, J.: Effects of injection nozzle exit width on rotating detonation engine. *Acta Astronaut.* **140**, 388–401 (2017)
8. Palaniswamy, S., Akdag, V., Peroomian, O., Chakravarthy, S.: Comparison between ideal and slot injection in a rotating detonation engine. *Combust. Sci. Technol.* **190**, 557–578 (2018)
9. Schwer, D., Kailasanath, K.: Numerical investigation of the physics of rotating-detonation-engines. *Proc. Combust. Inst.* **33**, 2195–2202 (2011)
10. George, S.: A., Driscoll, R., Anand, V., Gutmark, E.: on the existence and multiplicity of rotating detonations. *Proc. Combust. Inst.* **36**, 2691–2698 (2017)
11. Katta, V.R., Cho, K.Y., Hoke, J.L., Codoni, J.R., Schauer, F.R., Roquemore, W.M.: Effect of increasing channel width on the structure of rotating detonation wave. *Proc. Combust. Inst.* in press. **37**, 3575–3583 (2018). <https://doi.org/10.1016/j.proci.2018.05.072>
12. Gaillard, T., Davidenko, D., Dupoirieux, F.: Numerical optimisation in non reacting conditions of the injector geometry for a continuous detonation wave rocket engine. *Acta Astronaut.* **111**, 334–344 (2015)
13. Braun, J., Saracoglu, B.H., Paniagua, G.: Unsteady performance of rotating detonation engines with different exhaust nozzles. *J. Propuls. Power.* **33**, 121–130 (2017)
14. Tang, X.M., Wang, J.P., Shao, Y.T.: Three-dimensional numerical investigations of the rotating detonation engine with a hollow combustor. *Combust. Flame.* **162**, 997–1008 (2015)
15. Anand, V., Gutmark, E.: Rotating detonation combustors and their similarities to rocket instabilities. *Prog. Energy Combust. Sci.* **73**, 182–234 (2019)
16. Jourdaine, N., Tsuboi, N., Ozawa, K., Kojima, T., Koichi Hayashi, A.: Three-dimensional numerical thrust performance analysis of hydrogen fuel mixture rotating detonation engine with aerospike nozzle. *Proc. Combust. Inst.* **2018**, 3443–3451 (in press). <https://doi.org/10.1016/j.proci.2018.09.024>
17. Shao, Y.T., Liu, M., Wang, J.P.: Numerical investigation of rotating detonation engine propulsive performance. *Combust. Sci. Technol.* **182**, 1586–1597 (2010)
18. Shao, Y., Liu, M., Wang, J.: Continuous detonation engine and effects of different types of nozzle on its propulsion performance. *Chinese J. Aeronaut.* **23**, 647–652 (2010)
19. Yi, T.-H., Lou, J., Turangan, C., Choi, J.-Y., Wolanski, P.: Propulsive performance of a continuously rotating detonation engine. *J. Propuls. Power.* **27**, 171–181 (2011)
20. Yi, T.-H., Turangan, C., Lou, J., Wolanski, P., Kindracki, J.: A three-dimensional numerical study of rotational detonation in an annular chamber. In: 47th AIAA Aerospace Sciences Meeting including The New Horizons Forum and Aerospace Exposition. American Institute of Aeronautics and Astronautics (2009)
21. Yamada, T., Hayashi, A.K., Yamada, E., Tsuboi, N., Tangirala, V.E., Fujiwara, T.: Detonation limit thresholds in H_2/O_2 rotating detonation engine. *Combust. Sci. Technol.* **182**, 1901–1914 (2010)
22. Anand, V., St. George, A., Driscoll, R., Gutmark, E.: Longitudinal pulsed detonation instability in a rotating detonation combustor. *Exp. Therm. Fluid Sci.* **77**, 212–225 (2016)
23. Bluemner, R., Bohon, M., Paschereit, C.O., Gutmark, E.J.: Dynamics of counter-rotating wave modes in an RDC. 2018 Jt. Propuls. Conf. (2018)
24. Anand, V., George, S.: A., Driscoll, R., Gutmark, E.: characterization of instabilities in a rotating detonation combustor. *Int. J. Hydrog. Energy.* **40**, 16649–16659 (2015)
25. Liu, Y., Zhou, W., Yang, Y., Liu, Z., Wang, J., Liu, Y., Zhou, W., Yang, Y., Liu, Z., Wang, J.: Numerical study on the instabilities in H_2 -air rotating detonation engines numerical study on the instabilities in H_2 -air rotating detonation engines. *Phys. Fluids.* **046106**, (2018)
26. Liu, P., Li, Q., Huang, Z., Zhang, H.: Interpretation of wake instability at slip line in rotating detonation. *Int. J. Comput. Fluid.* **32**, 379–394 (2018)
27. Li, Q., Liu, P., Zhang, H.: Further investigations on the interface instability between fresh injections and burnt products in 2-D rotating detonation. *Comput. Fluids.* **170**, 261–272 (2018)

28. Yao, S.Z.S., Zhang, M.L.L.: Effects of injection conditions on the stability of rotating detonation waves. *Shock Waves*. **28**, 1079–1087 (2018)
29. Hishida, M., Fujiwara, T., Wolanski, P.: Fundamentals of rotating detonations. *Shock Waves*. **19**, 1–10 (2009)
30. Rachel M. Russo, King, P.I., Schauer, F.R., Thomas, L.M.: Characterization of Pressure Rise Across a Continuous Detonation Engine. 47th AIAA/ASME/SAE/ASEE Jt. Propuls. Conf. Exhib. AIAA 2011–6046 (2011)
31. St. George, A.C.: Development and testing of pulsed and rotating detonation combustors. PhD Thesis, University of Cincinnati, Cincinnati, USA (2016)
32. Schwer, D., Kailasanath, K.: Feedback into mixture plenums in rotating detonation engines. In: 50th AIAA Aerospace Sciences Meeting including the New Horizons Forum and Aerospace Exposition. American Institute of Aeronautics and Astronautics (2012)
33. Schwer, D., Corrigan, A., Taylor, B., Kailasanath, K.: On Reducing Feedback Pressure in Rotating Detonation Engines. In: 51st AIAA Aerospace Sciences Meeting including the New Horizons Forum and Aerospace Exposition. American Institute of Aeronautics and Astronautics (2013)
34. Levin, V.A., Manuylovich, I.S., Markov, V. V: Numerical simulation of rotating det-onation under variable conditions. The 26th International Colloquium on the Dynamics of Explosions and Reactive Systems (ICDERS), Boston, MA. (2017)
35. Sun, J., Zhou, J., Liu, S., Lin, Z., Lin, W.: Plume flowfield and propulsive performance analysis of a rotating detonation engine. *Aerosp. Sci. Technol.* **81**, 383–393 (2018)
36. Meng, Q., Zhao, N., Zheng, H., Yang, J.: Numerical investigation of the effect of inlet mass flow rates on H₂/air non-premixed rotating detonation wave. *Int. J. Hydrot. Energy*. **43**, 13618–13631 (2018)
37. Jasak, H.: Error analysis and estimation for the finite volume method with applications to fluid flows. PhD Thesis, Imperial College of Science, Technology and Medicine, London (1996)
38. Kurganov, A., Tadmor, E.: New high-resolution central schemes for nonlinear conservation laws and convection-diffusion equations. *J. Comput. Phys.* **160**, 241–282 (2000)
39. Kurganov, A., Noelle, S., Petrova, G.: Semidiscrete central-upwind schemes for hyperbolic conservation laws and Hamilton–Jacobi equations. *SIAM J. Sci. Comput.* **23**(3), 707–740 (2001)
40. Schwer, D.A., Kailasanath, K.: Effect of low pressure ratio on exhaust plumes of rotating detonation engines. In: 50th AIAA/ASME/SAE/ASEE Joint Propulsion Conference. American Institute of Aeronautics and Astronautics (2014)
41. Katta, V.R., Cho, K.Y., Hoke, J.L., Codoni, J.R., Schauer, F.R., Roquemore, W.M.: Effect of increasing channel width on the structure of rotating detonation wave. *Proc. Combust. Inst.* **37**, 3575–3583 (2019)
42. Shock & Detonation Toolbox, California Institute of Technology, http://www2.galcit.caltech.edu/EDL/public/cantero/html/SD_Toolbox. Accessed Sept 2018.
43. Marinov, N.M.: Westbrook, C.K., Pitz, W.J. Detailed and global chemical kinetics model for hydrogen, in *Transport Phenomena in Combustion* (1995)
44. Choi, J.-Y., Jeung, I.-S., Yoon, Y.: computational fluid dynamics algorithms for unsteady shock-induced combustion, part 1: validation. *AIAA J.* **38**, 1179–1187 (2000)
45. Berglund, M., Fedina, E., Fureby, C., Tegnér, J., Sabel'nikov, V.: Finite rate chemistry large-eddy simulation of self-ignition in supersonic combustion ramjet. *AIAA J.* **48**, 540–550 (2010)
46. Choi, J.-Y., Jeung, I.-S., Yoon, Y.: Computational fluid dynamics algorithms for unsteady shock-induced combustion, part 2: comparison. *AIAA J.* **38**, 1188–1195 (2000)
47. Slack, M.W.: Rate coefficient for H + O₂ + M = HO₂ + M evaluated from shock tube measurements of induction times. *Combust. Flame*. **249**, 241–249 (2000)
48. Conaire, M., Curran, H.J., Simmie, J.M., Pitz, W.J., Marcus, O., Westbrook, C.K.: A comprehensive modeling study of hydrogen oxidation. *Int. J. Chem. Kinet.* **36**, 603–622 (2004)
49. Desbordes, D.: Stationary and Transient Aspects of Detonation in Gases: Relationship with the Cellular Structure of the Forehead, (1990)
50. Strehlow, R.A., Engel, C.D.: Transverse waves in detonations: II. structure and spacing in H₂-O₂, C₂H₂-O₂, C₂H₄-O₂, and CH₄-O₂ Systems. *AIAA J.* **7**, 323–328 (1969)
51. Zitoun, R., Desbordes, D., Guerraud, C., Deshaies, B.: Direct initiation of detonation in cryogenic gaseous H₂-O₂ mixtures. *Shock Waves*. **4**, 331–337 (1995)
52. Rankin, B.A., Richardson, D.R., Caswell, A.W., Naples, A., Hoke, J., Schauer, F.: Imaging of OH* chemiluminescence in an optically accessible nonpremixed rotating detonation engine. In: 53rd AIAA Aerospace Sciences Meeting. American Institute of Aeronautics and Astronautics (2015)
53. Goodwin, G.B., Oran, E.S.: Premixed flame stability and transition to detonation in a supersonic combustor. *Combust. Flame*. **197**, 145–160 (2018)

54. Houim, R.W., Fievisohn, R.T.: The influence of acoustic impedance on gaseous layered detonations bounded by an inert gas. *Combust. Flame.* **179**, 185–198 (2017)
55. Li, L., Li, J.-M., Nguyen, V.B., Teo, C.J., Chang, P.-H., Khoo, B.C.: A study of detonation re-initiation through multiple reflections in a 90-degree bifurcation channel. *Combust. Flame.* **180**, 207–216 (2017)
56. Yao, S., Ma, Z., Zhang, S., Luan, M., Wang, J.: Reinitiation phenomenon in hydrogen-air rotating detonation engine. *Int. J. Hydrot. Energy.* **42**, 28588–28598 (2017)
57. Ma, Z., Zhang, S., Luan, M., Yao, S., Xia, Z., Wang, J.: Experimental research on ignition, quenching, reinitiation and the stabilization process in rotating detonation engine. *Int. J. Hydrot. Energy.* **43**, 18521–18529 (2018)
58. St. George, A.C., Driscoll, R.B., Anand, V., Gutmark, E.J.: Starting transients and detonation onset behavior in a rotating detonation combustor. In: 54th AIAA Aerospace Sciences Meeting. American Institute of Aeronautics and Astronautics (2016)